Review Article

Metal additive manufacturing for particle accelerator applications

Tobia Romano,[1,2,*] Guntis Pikurs,[2,3] Andris Ratkus,[2] Toms Torims,[2,3] Nicolas Delerue,[4] Maurizio Vretenar,[3] Lukas Stepien,[5] Elena López,[5] and Maurizio Vedani[1]

[1]*Department of Mechanical Engineering, Politecnico di Milano, 20156 Milan, Italy*
[2]*Institute of Particle Physics and Accelerator Technologies, Riga Technical University, LV-1048 Riga, Latvia*
[3]*The European Organization for Nuclear Research (CERN), 1211 Meyrin, Switzerland*
[4]*Laboratoire de Physique des 2 Infinis Irène Joliot-Curie (IJCLab), 91400 Orsay, France*
[5]*Fraunhofer Institute for Material and Beam Technology, IWS, Winterbergstraße 28, 01277 Dresden, Germany*

(Received 22 February 2024; accepted 23 April 2024; published 17 May 2024)

Metal additive manufacturing technologies are rapidly becoming an integral part of the advanced technological portfolio for the most demanding industrial applications. These processes are capable of fabricating three-dimensional components with near-net shape quality by depositing the constituent materials in a layer-by-layer fashion. This fabrication approach provides numerous advantages over conventional manufacturing methods, including enhanced design flexibility, reduced production costs and lead times, rapid prototyping, and the possibility to repair damaged parts. In recent years, the growing demand for novel accelerator components with improved performance characteristics, integrating structures such as drift tubes and internal cooling channels, has prompted the exploration of additive manufacturing in the field of particle accelerators. Radio-frequency components, beam intercepting devices, and vacuum systems have been prototyped using various metallic materials and additive manufacturing technologies, demonstrating performance levels comparable to the conventionally manufactured counterparts in preliminary tests. However, the absence of established qualification protocols and the uncertain reliability of additively manufactured parts under the demanding conditions typical of accelerator applications pose significant challenges to the integration of additive manufacturing processes into the fabrication practices of these components. This paper provides a comprehensive review of documented applications of metal additive manufacturing in particle accelerators, highlighting benefits, challenges, and opportunities for future improvements. The main requirements and currently available test setups for the assessment of additively manufactured components in applications involving ultrahigh vacuum and intense electromagnetic fields are also discussed.

DOI: 10.1103/PhysRevAccelBeams.27.054801

I. INTRODUCTION

Particle accelerators play a crucial role across various scientific disciplines, including fundamental physics and materials science [1,2], and practical applications, such as radiation therapy for cancer treatment, ion implantation in electronics, and food sterilization [3–5]. According to the International Atomic Energy Agency (IAEA), over 30,000 accelerators are currently in operation worldwide [6].

The increasing deployment of accelerator facilities in diverse fields of applied science has raised the demand for innovative technologies to meet current needs for compact designs, increased energy efficiency, and reduced commissioning and maintenance costs [7]. This has prompted the exploration of novel accelerator component concepts boasting superior performance characteristics to enable a new generation of resource-efficient devices with extended operating times and capable of pushing beyond the current energy frontiers, to pave the way for new discoveries in particle physics research [8,9].

The development of novel designs for complex accelerator components with enhanced performance, incorporating structures such as drift tubes, vacuum connectors, and cooling channels, has required the adoption of advanced manufacturing routes involving several fabrication steps and highly skilled labor for precise machining and joining operations [10,11]. In this context, the opportunity to integrate metal additive manufacturing (AM) technologies into the fabrication practices of accelerator

*Corresponding author: tobia.romano@polimi.it

components has emerged in the past few years, aiming to simplify the production processes, reduce costs and lead times, and eliminate the design constraints imposed by conventional methods [7,12].

AM processes create three-dimensional objects by depositing the constituent materials layer after layer, following the geometry outlined in computer-aided design (CAD) models. This approach enables the one-step fabrication of complex structures with a near-net shape quality, opening up possibilities for topological optimization based on the functional requirements of the intended component, no longer limited by technology-related restrictions [13]. These may include, for example, the integration of conformal cooling channels for enhanced thermal efficiency and lattice structures to minimize weight and material usage while providing adequate structural properties. In AM, geometric complexity is not usually associated with significantly higher production costs. Moreover, it is particularly suited for rapid prototyping and for the production of one-off parts and limited series, as is frequently the case for accelerator components designed for specific particle beam characteristics [9]. In contrast, the fabrication of complex parts with conventional methods often entails multiple expensive and time-consuming machining and joining operations. The large amount of scrap produced during machining is particularly impactful for parts made from expensive raw materials, such as niobium superconducting radio-frequency (SRF) cavities [14]. Additionally, the production of small batches may not warrant the initial investment for dedicated molds and tools. Figure 1 qualitatively compares the unit cost as a function of part complexity and production volume for AM and conventional manufacturing methods.

The monolithic fabrication of seamless structures enabled by AM can improve component reliability by preventing possible misalignments and the formation of detrimental phases at interface regions during joining operations. This holds particular relevance for rf applications, where surface discontinuities can compromise device performance [16]. The demonstrated capability of AM to repair high-value industrial components further emphasizes its potential [17]. Since accelerator components account for a significant portion of the overall cost of accelerator facilities [9,18], repair opportunities through AM methods may be considered aiming at reducing the maintenance expenses.

Major challenges to the integration of metal AM technologies into the manufacturing routes of accelerator components are related to the absence of established protocols for qualification, the uncertain reliability of parts produced by AM under the demanding service conditions often encountered in accelerator applications, and the still open questions regarding the process-microstructure-property relationship in additively manufactured parts. The latter aspect is still the subject of ongoing scientific research due to the multitude of experimental parameters and postprocessing operations that can influence the quality of parts produced by AM, including surface roughness, thermal stresses causing deformations in printed parts, peculiar microstructures, and defects developing from the complex physical phenomena involved in the processes [15,19,20]. An additional source of the challenge is the increasing demand for design expertise to fully leverage the flexibility of AM through topological optimization based on mechanical, thermal, thermodynamic, electromagnetic, and beam dynamics simulations, pursuing the so-called design for AM paradigm [21].

Despite these challenges, there are specific scenarios in which AM can offer considerable advantages for the manufacturing of particle accelerator components over conventional fabrication methods. This work provides a comprehensive review of applications of metal AM in the accelerator sector, documenting the benefits and challenges evidenced to date in the literature.

II. METAL ADDITIVE MANUFACTURING TECHNOLOGIES

Metal AM technologies can be divided into single-stage and multistage processes [22]. In single-stage processes,

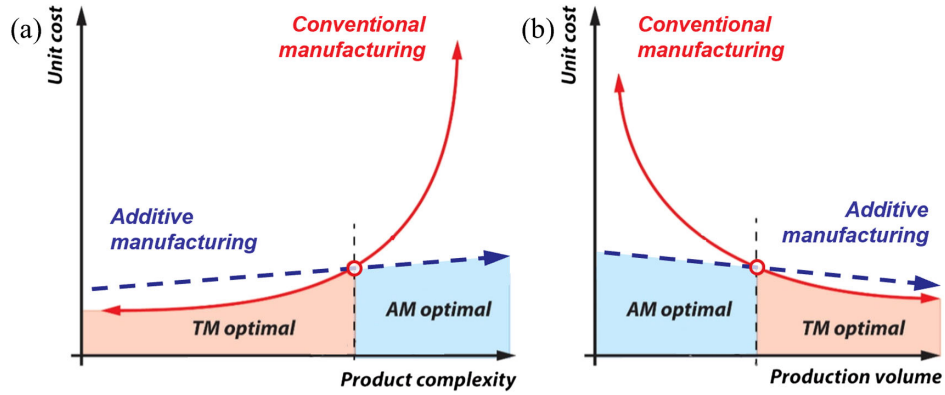

FIG. 1. Unit cost as a function of (a) part complexity and (b) production volume for AM and conventional manufacturing methods [15].

parts with the basic geometry and material properties are manufactured in a single operation starting from a feedstock material in the form of powder or wire. On the other hand, multistage processes typically involve an initial printing operation providing the basic geometry of the desired product, followed by consolidation procedures to impart the required structural integrity and properties.

A. Single-stage processes

Depending on the material feeding strategy, the most established single-stage (or direct) metal AM processes can be classified as powder bed fusion (PBF) and direct energy deposition (DED). Both classes include techniques that can process various metallic materials, such as iron, aluminum, titanium, nickel, and copper alloys, as well as precious and refractory metals.

In PBF processes, the powder feedstock is spread onto a build platform in layers of controlled thickness to generate a so-called powder bed. After the deposition of each layer, a heat source selectively melts the powder according to the designed model to build a three-dimensional part layer by layer. The process is called laser beam powder bed fusion of metals (PBF-LB/M) [27] or electron beam powder bed fusion (PBF-EB) depending on the nature of the heat source used.

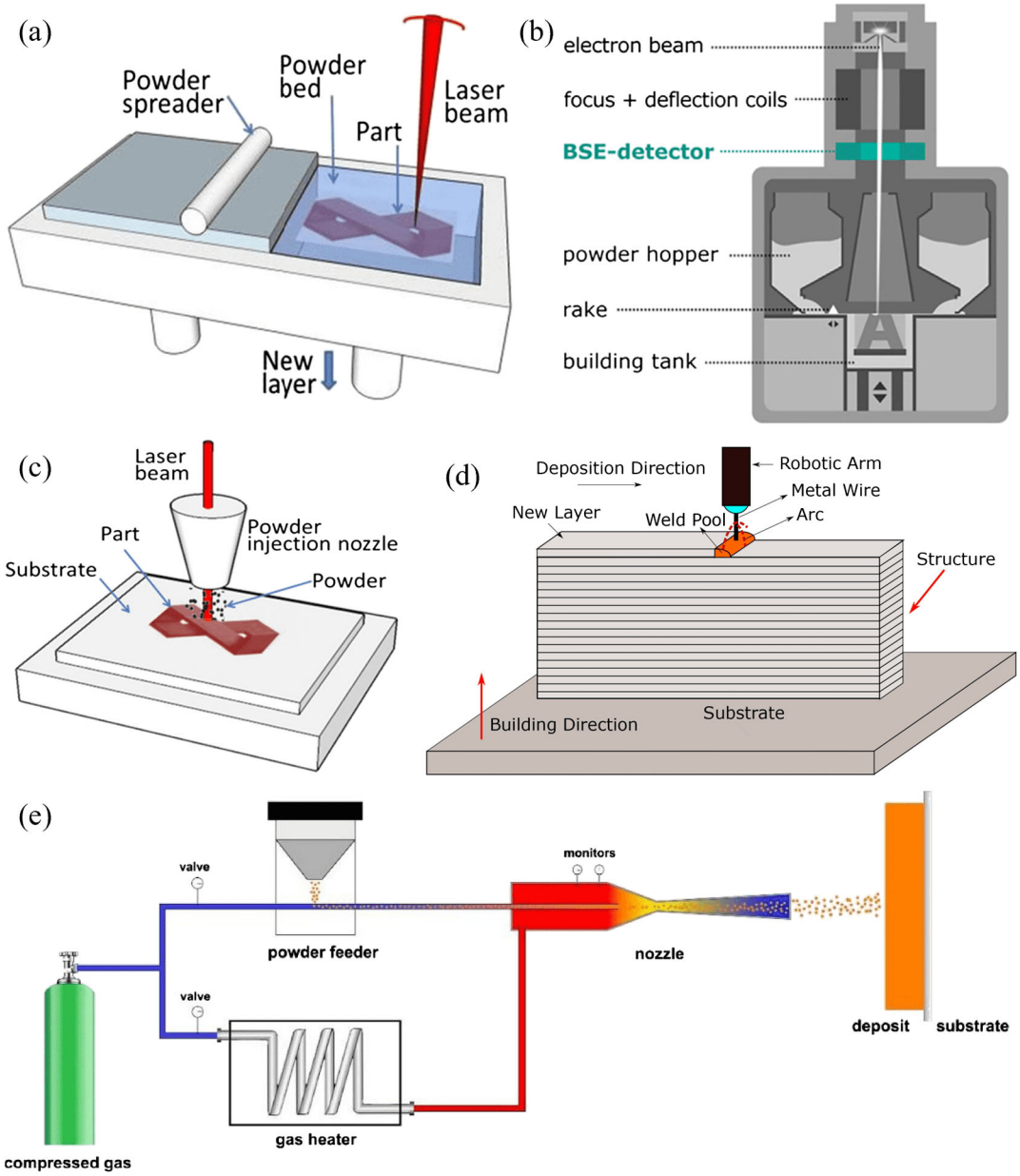

FIG. 2. Schematic diagrams of single-stage AM processes: (a) PBF-LB/M [23], (b) PBF-EB [24], (c) LMD [23], (d) WAAM [25], and (e) CSAM [26].

In PBF-LB/M [Fig. 2(a)], the printing procedure is usually conducted inside a closed chamber filled with inert gas to prevent material contamination. The use of highly focused laser beams (∼30–100 μm spot size), fine powders ranging from 5 to 60 μm in size, and layer thicknesses generally below 50 μm allows realizing minute details with a resolution of up to 0.2–0.4 mm [15,28,29]. In recent years, commercial machines with large build volumes also became available for the fabrication of parts with up to 800 mm base diameter and 850 mm height [29]. Most systems are equipped with one or multiple infrared laser sources with a wavelength of around 1000 nm and a maximum power of up to 1 kW, suitable for the processing of most engineering metallic materials. However, highly reflective metals, like pure copper, exhibit a limited absorption rate in the infrared range (Fig. 3) [30], which often results in defects in the printed parts due to incomplete fusion of the powder [31]. High laser powers (1 kW or higher) can be used to compensate for the low absorption [32–34]. PBF-LB/M machines using green laser sources have also been developed to improve the processability of materials with maximum absorbance in this wavelength range [35,36].

In PBF-EB [Fig. 2(b)], the use of a high-energy electron beam requires the printing process to occur in vacuum, ensuring a high material purity. The electron beam is scanned across the powder bed using magnetic coils, which can move it almost instantaneously by properly varying the input parameters [37]. This aspect, combined with the very effective absorption of the beam energy by the powder material, results in higher production rates compared to PBF-LB/M, as complete fusion is guaranteed even when selecting high scanning speeds [23]. In order to prevent a negative electric charge from accumulating on the surface

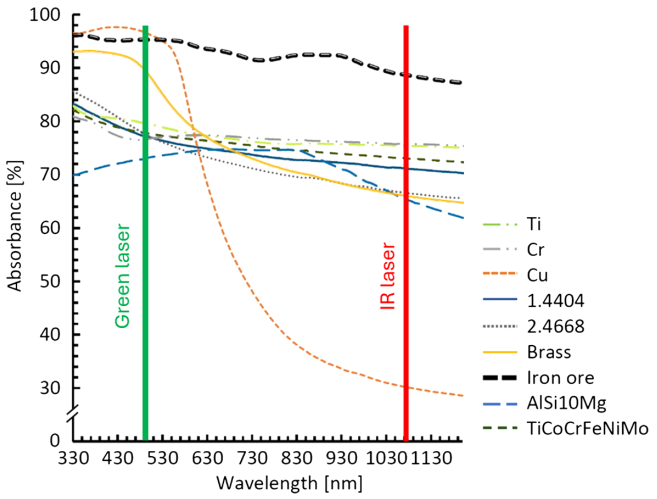

FIG. 3. Absorbance of metal powders as a function of laser wavelength; the green and red lines indicate typical green ($\lambda = 515$ nm) and IR ($\lambda = 1070$ nm) laser wavelengths, respectively, employed in commercial PBF-LB/M machines [30].

of the powder bed, each layer is preheated by the electron beam at high power and high scanning speed. Preheating is beneficial for materials sensitive to hot cracking, which require relatively longer times at high temperatures and slower cooling rates to ensure defect-free parts upon solidification. In addition, the preliminary electron beam scans partially sinter the powder particles before the actual selective melting procedure. The slightly consolidated powder bed provides an electrical connection for better charge dissipation and can serve as a support for the creation of inclined overhang structures at angles that cannot be achieved by PBF-LB/M without the use of supports conveniently included in the model. However, it results in a high surface roughness of as-printed parts [38]. This effect is further accentuated by the preferred use of relatively coarse powders (typically, 45–100 μm [39]), having a lower tendency to be ejected from the powder bed due to electrostatic repulsion. The maximum build volume of commercially available PBF-EB systems is comparable to that of PBF-LB/M machines, with a 350 mm base diameter and 380 mm height [15].

In DED processes, the feedstock material in powder or wire form is simultaneously melted by a focused heat source (laser beam, electron beam, or electric arc) while it is being deposited only in the desired locations with a nozzle system. Examples of DED technologies include laser metal deposition (LMD), which employs a coaxial nozzle equipped with a laser source to melt the material fed to the molten region [Fig. 2(c)], and wire arc additive manufacturing (WAAM), which uses an electric arc to deposit metallic filaments [Fig. 2(d)]. Compared to PBF, DED techniques can fabricate larger freeform parts because the printing process does not necessarily require an enclosed work chamber. The direct deposition approach is also suitable for printing additional features on existing parts without the need for a flat base surface and it opens up the possibility to repair high-value components and fabricate multimaterial structures by varying the composition of the material fed during the deposition process [40,41]. Although DED technologies usually have a lower resolution compared to PBF methods (∼1 mm minimum feature size [15]), the deposition head can be combined with milling tools to machine finer features and mechanically finish the as-printed surfaces as the part is built up layer after layer, thus alternating printing and milling operations [42].

A single-stage AM method similar to DED processes, but not involving the complete melting of the powder feedstock material, is cold spray additive manufacturing (CSAM). During the process, fine metal or ceramic powders are accelerated within a compressed gas stream toward a substrate (a build platform for fabricating standalone parts or an existing component for feature addition or repair). Upon high-velocity impact on the substrate surface, the particles plastically deform and bond together,

generating a layer of consolidated material [Fig. 2(e)]. CSAM features high material efficiency and low energy consumption. It can provide certain design flexibility through configurations that allow the motion of both the spray gun and the substrate. Similar to DED techniques, it also enables the fabrication of discrete, functionally graded, and even metal-ceramic multimaterial parts by varying the powder composition during the process [43,44].

B. Multistage processes

Multistage (or indirect) AM processes include different technologies which, unlike direct processes, usually do not involve the complete melting and solidification of the initial material. Among them, it is worth mentioning bound metal deposition (BMD) and ultrasonic additive manufacturing (UAM), which have already been studied for applications in the field of particle accelerators [45,46].

BMD uses wax and polymer filaments loaded with a metallic powder as feedstock material. A deposition head heats the filament to make it fluid and deposits it onto a build plate to create a three-dimensional part layer after layer. The printing operation is followed by high-temperature debinding and sintering to remove the polymeric fraction and consolidate the metal powder, respectively [Fig. 4(a)]. The slow and uniform heating of the material during the sintering step results in stress-free products. On the other hand, residual porosity is often observed in the sintered parts [49] and impurities produced by incomplete combustion of the polymer may affect the material properties.

UAM is a hybrid process that combines ultrasonic-assisted welding and computer numerical control machining. Three-dimensional parts are built by stacking thin metal foils (∼100–150 μm thickness [50]) welded together using a sonotrode. The strong interface friction generated by the rotating and vibrating sonotrode induces plastic deformation and intimate contact between the metal foils, resulting in metallurgical bonding. After stacking a certain number of foils, a machine tool is used to trim the deposit to create one slice of the designed part [Fig. 4(b)]. This alternation of additive and subtractive operations is repeated until achieving the final geometry. One advantage of UAM is that accuracy and surface quality do not depend on the thickness of the metal foils used, but only on the machining tool and strategy adopted. Inclined and curved surfaces can be easily milled, faithfully reproducing the geometry of the component model. Also, thanks to the building approach based on foil piling, multifunctional parts made of multiple materials or embedded electronic components like fiber optics and sensors can be manufactured.

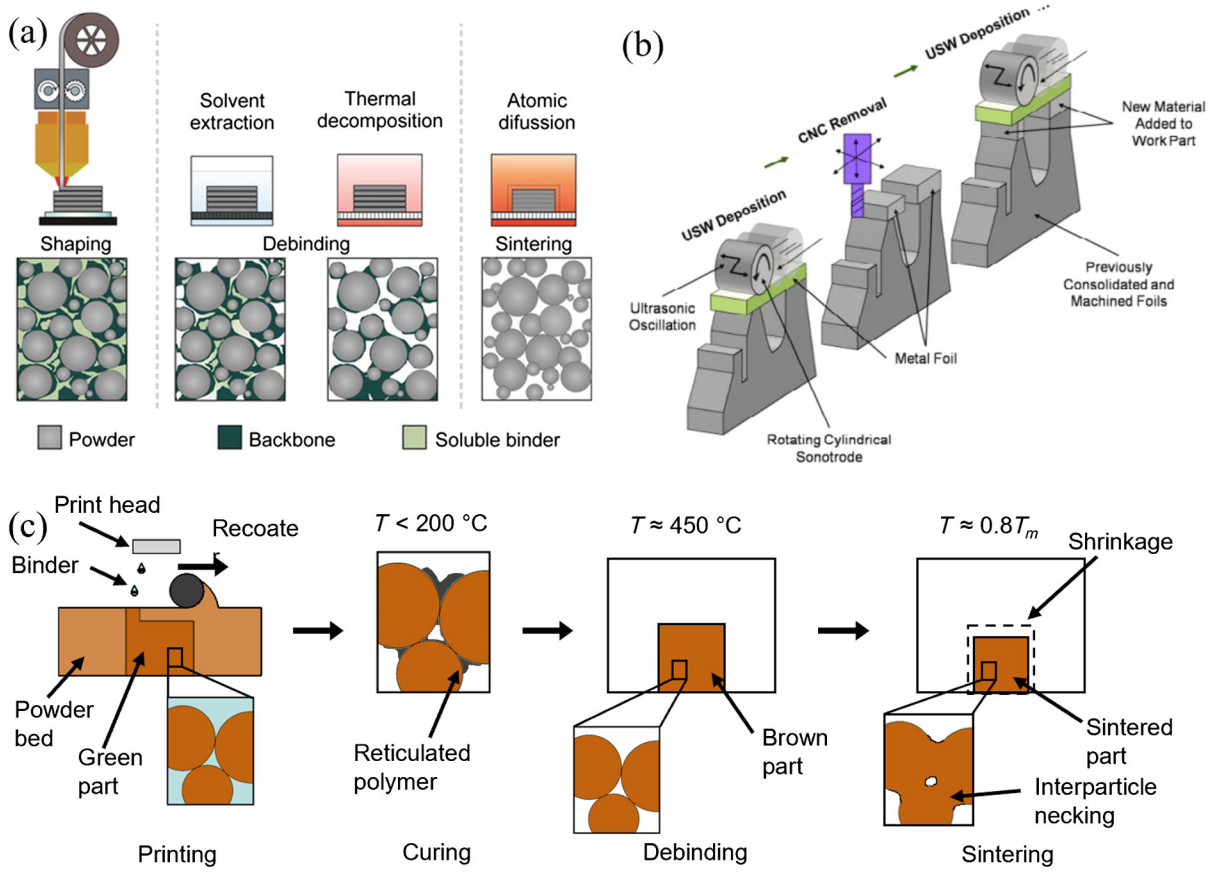

FIG. 4. Schematic diagrams of multistage AM processes: (a) BMD [47], (b) UAM [48], and (c) BJT [38].

However, very complex geometries and overhanging elements cannot usually be integrated into the design due to the inherent lack of support structures [50].

Another indirect AM technology that has experienced rapid development in recent years for the processing of both metallic and ceramic materials is binder jetting (BJT) [51]. BJT is based on the same powder bed approach of PBF processes. However, a print head selectively deposits a polymeric binder to join the powder particles in each powder layer and between adjacent layers, instead of melting them with a high-energy beam. Following the printing step, the so-called green parts are first subjected to a curing treatment at a moderate temperature to reticulate the binder and provide sufficient mechanical strength for handling operations [38]. Then, high-temperature debinding and sintering cycles are applied to burn off the polymer and densify the material [Fig. 4(c)], like in the BMD process. Unlike PBF methods, the powder bed can support overhang elements during the BJT process, eliminating the need for further support structures [52]. Several parts can also be printed stacked on top of each other in a single job, resulting in higher productivity and lower fabrication costs [51]. The main challenges are to obtain fully dense products from green parts, with typical relative densities of around 50%, and to control the size and geometry of the components during densification to ensure a good accuracy [52,53].

III. METALLIC MATERIALS FOR ACCELERATOR APPLICATIONS

The variety of metallic materials used in the fabrication of accelerator components is not very large [54]. It mainly includes pure copper and copper-based alloys, niobium and other superconducting materials, stainless steel, aluminum alloys, titanium alloys, nickel-based alloys and superalloys, and refractory metals. Many of these materials are commercially available as feedstock for various AM systems and have already been studied in this framework in terms of processability and achievable properties [15,23,55].

A. Pure copper and copper alloys

High-purity copper is used for the fabrication of several accelerator components, such as rf cavities and quadrupoles, waveguides, vacuum seals, klystrons, and various types of cathodes [56–60] because it has excellent electrical and thermal properties, good formability, workability and solderability, and a relatively high corrosion resistance. The combination of high thermal conductivity and low electrical resistivity is crucial for increasing the sustainable electric fields in high-gradient normal-conducting accelerators, in order to enhance efficiency and avoid overheating caused by ohmic losses, which can cause significant thermal expansion and distortions that can change the rf phase response of the accelerating structures [61,62]. Pure copper grades that are typically used in accelerator applications are oxygen-free (OF, >99.95% Cu) and oxygen-free electronic (OFE, >99.99% Cu) copper, having a low outgassing tendency [63] due to the stringent limits on the content of oxygen and other impurities. OFE copper is preferred in cryogenic applications requiring a large residual resistivity ratio (RRR) [56].

A limitation of pure copper is that its mechanical properties degrade at relatively low temperatures (softening already occurs around 250 °C [64]). For this reason, copper alloys with better mechanical properties are often preferred in applications involving thermal cycling and pulsed heating. The long straight sections (LSS) of the drift chambers of the vacuum system of the Large Hadron Collider (LHC) were manufactured in C10700 Cu-Ag alloy because the inner walls were coated by a nonevaporable getters (NEG) coating having an activation temperature in the range of 200–300 °C [56]. A small addition of silver (0.085%) can in fact improve softening and creep resistance of the base material while keeping comparable electrical and thermal properties [63,64]. Precipitation-hardening CuCr, CuZr, and CuCrZr alloys also exhibit higher hardness and strength, resulting in low susceptibility to surface damage during pulsed heating [65]. Excellent high-temperature performance is also shown by oxide dispersion-strengthened (ODS) coppers, in which nanometric ceramic particles reinforce the metal matrix. Alumina-reinforced Glidcop® has been used to fabricate crotches for the absorption of synchrotron radiation [64] and is normally employed when vacuum brazing is required [66] as the finely dispersed particles prevent recrystallization and softening of the copper matrix even at typical brazing temperatures (∼600 °C) at which precipitation-hardening alloys start becoming unstable [56]. However, in these systems, the gain in mechanical properties is inevitably accompanied by a slight reduction in the electrical conductivity.

B. Niobium and niobium-based superconducting systems

Pure niobium (>99.95% Nb) is primarily used to manufacture rf cavities and magnets for superconducting accelerator facilities [67] since it is able to generate very high accelerating electric fields with little heat dissipation. Historically, niobium has been used for these applications because, among pure metals, it has the highest critical temperature (∼9.2 K), the highest lower critical magnetic field, and the highest superheating field [68]. It also features good formability and can be easily molded into cavity shapes [69]. Copper cavities internally coated with a thin film of pure niobium have also been developed since the 1980s [70] and employed at CERN in several experiments [71]. Such structures offer some advantages over bulk niobium cavities, including the reduction of costs associated with both raw materials and manufacturing

routes and a better thermal stability, resulting from the superior thermal conductivity of copper, and the easier implementation of optimally designed cryomodules [68,70,72]. Nb-Ti alloy and Nb_3Sn intermetallics are also used for the fabrication of superconducting joints, wires, and Rutherford cables [73–75].

C. Stainless steel

Stainless steel is a crucial material for the construction of new generation accelerators [56]. It is widely employed to manufacture waveguides, beampipes, flanges, and vacuum connectors, as well as structural components also working at cryogenic temperatures, like the standard dipole magnet collars of the LHC [76–79]. The grades mainly used in accelerator applications are 304L and 316L austenitic stainless steels because they combine high strength, ductility, toughness, and corrosion resistance. They can also be easily machined to create the sharp edges typically required in vacuum seals [56]. A major limitation is that the metastable austenitic phase is susceptible to martensitic transformation when cooled to cryogenic temperatures. Martensite has a higher magnetic susceptibility compared to austenite and is brittle at cryogenic temperatures. 304L steel suffers from martensitic transformation already at liquid nitrogen temperature (∼77 K) [79]. Small additions of nitrogen can significantly increase austenite stability against martensitic transformation in 316L. Nitrogen-strengthened 316LN steel with ∼0.2% N content can retain a large ductility even at liquid helium temperature (∼4 K) [79,80]. The superior corrosion resistance and resistance to softening of 316LN also make it suitable for vacuum-firing operations, i.e., heating the component at ∼1000 °C for several hours to remove dissolved gases (mainly hydrogen) and improve its outgassing performance [81].

D. Pure aluminum and aluminum alloys

Pure aluminum and aluminum alloys are largely employed to manufacture waveguides, microwave cavities, and casings for superconducting quantum devices [82–86]. Aluminum combines good electrical and thermal properties with a higher transparency to radiation and a lower residual radioactivity compared to other structural materials like copper and stainless steel [56,87]. Depending on their chemical composition, aluminum alloys can be plastically deformed or welded to produce parts with relatively complex geometry. However, their use should be carefully considered for components subjected to high temperature cycles, such as vacuum chambers undergoing firing and NEG coating activation, as they may suffer from temperature-induced softening and creep [56].

E. Titanium alloys

Titanium alloys find many structural applications in high-energy physics facilities because they combine good mechanical properties, like specific strength, ductility, and fatigue endurance limit, with excellent high-temperature stability and corrosion resistance [15,88]. Their relatively low elastic modulus and coefficient of thermal expansion also result in a high resistance to thermal shocks induced by pulsed beams, making them a preferred material for beam dumps and windows [89,90]. Since they do not show ductile-to-brittle transition at low temperatures [91], various titanium grades have been used to produce liquid helium storage vessels and cryomodules for cryogenic cooling of superconducting accelerator components [92–94].

Ti-45Nb alloy is often employed to manufacture type-II superconducting magnets and wires because it is more affordable than pure niobium while offering an accessible critical temperature (∼10 K), a high upper critical magnetic field, and a high critical current density [95]. Due to its higher mechanical properties [96], it is also preferred to unalloyed niobium for making flanges and connectors in multicell superconducting cavities [97].

F. Nickel alloys and superalloys

Nickel-based alloys are high-performance materials often used in demanding applications, as they display excellent mechanical properties, high creep resistance, and good corrosion resistance even in harsh environments [15,98]. Nickel superalloys are one of the main materials of choice for beam windows [99,100], because they retain high strength and ductility even after exposure to intense irradiation, resulting in great window durability and resistance to high dose levels for high-power beam applications [101–103]. They are also used to produce high-strength support frames to be integrated with superconducting coil structures [104]. Thanks to their high magnetic permeability, which is maintained even at cryogenic temperatures [105], Ni-Fe alloys are the preferred material for passive magnetic shielding of superconducting cavities cooled with liquid helium [106,107].

G. Refractory metals and alloys

Besides niobium, other refractory metallic materials are of particular interest for high-energy accelerator facilities. Refractory metals, such as tungsten, molybdenum, and tantalum, feature an extremely high melting point (well above 2000 °C) and can exhibit an excellent performance under various extreme conditions. Tungsten and molybdenum have been studied for the manufacturing of components directly exposed to high-energy beams, like beam intercepting devices [108], while tungsten-copper alloys are often employed for arcing contacts in high-voltage circuit breakers [109]. The materials used in these applications must withstand extreme thermomechanical stresses, as well as resist radiation damage. Tungsten, molybdenum, and tantalum find applications as electrode materials in high-voltage devices, such as ion sources and traveling wave tubes [110,111], and in high accelerating gradient and

high rf power structures [112,113] because they can guarantee low breakdown rates during operation [114]. Molybdenum and tantalum are also widely employed in electron guns due to their good thermal conductivity and dimensional stability [115]. Various combinations of refractory metals and alloys are good candidates as antiproton target materials because their high density allows the production of compact targets that prevent antiproton reabsorption into the surrounding material [116].

IV. REQUIREMENTS FOR ACCELERATOR COMPONENTS

Due to the extreme conditions to which accelerator components are often subjected during operation, there are several stringent requirements that the materials used in their production have to fulfill. This translates into a long list of aspects that need to be considered for the qualification of AM technologies for accelerator applications. They can be grouped into three key categories, relating, respectively, to the material properties, the manufacturing process, and the specific service conditions to which accelerator components are exposed.

A. Material properties

1. Chemical composition and purity

Materials used in particle accelerators usually have a tightly controlled chemical composition. Many applications require the use of pure metals with stringent limits on the impurity content, as they can dramatically alter the properties of the base material. For example, small contents of oxygen, carbon, and especially phosphorus can significantly reduce the thermal and electrical conductivity of copper [52,55,117], while hydrogen degrades the performance of superconducting niobium cavities by forming hydride precipitates that act as normal-conducting sites [118,119]. The quality factor (Q-factor) of niobium cavities is also affected by magnetic impurities, which cause inelastic scattering of the Cooper pairs and increase the surface resistance [120], thus locally increasing the rf losses and suppressing superconductivity. The number of contaminants prone to activation should be minimized in components exposed to irradiation to avoid the uncontrolled generation of radionuclides with a long half-life, which may cause safety concerns during maintenance and disposal [121]. Contaminants are a major source of outgassing in ultrahigh vacuum (UHV) systems [122], while surface impurities may promote vacuum electrical breakdown in high-voltage applications due to local field enhancement [123].

Achieving a well-controlled chemical composition in additively manufactured parts is often challenging, due to both feedstock quality and contamination or uncontrolled changes in element concentration that can occur during the fabrication process. Keeping the oxygen content within specifications is particularly critical in powder-based AM processes because oxidation can already occur during powder production, sieving, transport, and handling due to the high surface area of powder particles [117,124]. The pickup of impurities during PBF processing of sensitive materials, like titanium and aluminum alloys, can be limited by minimizing the content of residual oxygen and other contaminants in the build chamber [125]. In DED processes, however, this is more challenging because the shielding gas only provides a partial protection during material deposition [38,126]. The reuse of powder collected from previous printing operations should be approached with caution because the content of interstitial elements usually increases with each successive print cycle [127]. Special attention should also be paid to the possible loss of volatile elements, like zinc and magnesium, in processes that use high-energy beams, as selective vaporization may alter the chemical composition of the printed parts compared to the initial feedstock material [128].

2. Microstructure

A homogenous microstructure is a key requirement for accelerator components, as it provides increased formability, which is particularly important when the manufacturing process involves severe plastic deformation operations [129] and uniform mechanical and physical properties. These are crucial to avoid hot spots that may arise due to localized variation in electrical resistivity or thermal conductivity, as well as having a beneficial effect on the thermo-mechanical fatigue behavior of components exposed to pulsed beams [130]. In UHV applications, products with fine and uniform grain size distribution are mandatory, especially when the design involves thin-walled regions [56]. Microstructural anisotropy should also be avoided to ensure consistent thermal expansion properties, thus preventing the buildup of severe internal stresses during temperature fluctuations. In superconducting systems, local textures with low electron work function (like $\langle 100 \rangle$ fiber in pure niobium) may compromise the device efficiency [131]. In applications that involve high accelerating gradients, when using multiphase alloys, the different phases should be intimately mixed to prevent breakdown from occurring selectively at the dielectrically weaker phase [132].

Although the specific grain morphology depends on the nature of the material and the selected process parameters, it is not common to observe homogeneous microstructures in parts produced with the most established metal AM technologies due to their inherent layer-by-layer approach. In direct processes, relatively large columnar grains typically develop along the build direction and can traverse several layers. This may result in markedly different mechanical and physical properties along different directions [133].

3. Defects

Accelerator components must comply with strict limits on defect content. Porosity and nonmetallic inclusions should be minimized as they affect thermal, electrical, and mechanical properties of metallic materials. A high porosity may also compromise the outgassing performance in UHV applications [134], while relatively large inclusions may cause leakages [56]. Manufactured parts should also be free of residual stresses to prevent uncontrolled deformations that deviate from the geometric tolerances specified in the design and to ensure a high dimensional stability even for components subjected to high thermomechanical loads.

Typical defects observed in additively manufactured parts are gas porosity and the so-called lack-of-fusion. Round pores may be generated from gas entrapped in the feedstock material or absorbed during the printing process by the molten material [Fig. 5(a)], while lack-of-fusion defects are caused by incomplete melting of the powder and appear as irregularly shaped cavities [Fig. 5(b)] [23]. When employing high power densities and low scanning speeds in PBF-LB/M, the melting of the material can occur through keyhole formation. A keyhole is a deep and narrow cavity generated by the rapid evaporation of the metallic material, which pushes the surrounding melt enabling penetration and multiple reflections of the laser beam [135]. Although this results in excellent laser absorption efficiency, without careful control of the process parameters, the keyhole can become unstable and repeatedly collapse during the scanning process, producing round voids in the deposit due to entrapped vapor [Fig. 5(c)] [23].

Cracking may also occur if the process parameters are not properly adjusted, especially in the most crack-sensitive alloys. Delamination, as well as macroscopic distortion and geometrical inaccuracies, may result from thermal stresses developing during single-stage AM processes. Nonuniform and time-dependent stresses are generated from the repeated heating and cooling cycles the material experiences during the printing process. Understanding the evolution of these stresses, also by means of multiphysics simulations, is crucial to optimize part design and support structure configuration to improve heat dissipation and reduce distortions [23].

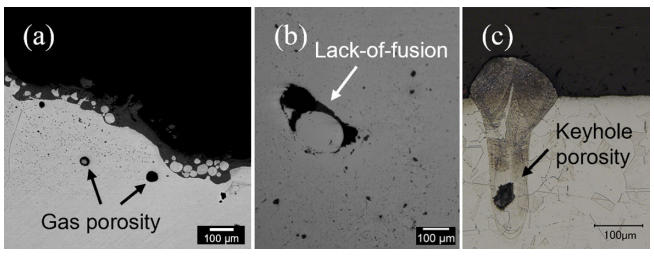

FIG. 5. (a) Gas-induced pores [126], (b) lack-of-fusion defect [42], and (c) keyhole-induced porosity [136] observed in additively manufactured deposits.

B. Manufacturing process

The characteristics of parts made by AM significantly depend on the technology and the process parameters employed. While PBF processes can provide superior dimensional accuracy, the limited volume of the build chamber of most commercially available systems may be insufficient for the fabrication of large accelerator components. On the other hand, DED and multistage processes do not usually have strict dimensional constraints but at the expense of resolution and design freedom.

Meeting the stringent surface roughness requirements typical of accelerator components poses a significant challenge for most available AM processes. The surface quality of additively manufactured parts in as-built conditions results from the interaction of a large number of factors related to feedstock material, part design, production technology, and process parameters [23,137]. A major source of surface roughness common to most AM methods is the so-called staircase effect, which results from converting three-dimensional models into stacks of discrete layers that approximate the ideal surface contour by steps [Fig. 6(a)] [138]. The staircase effect can be mitigated by reducing the layer thickness, which, however, increases the overall processing time, and by properly orienting the part to avoid highly inclined surfaces relative to the build direction [137]. In powder-based processes, another contribution to roughness comes from powder particles that adhere and partially sinter on the surface of the consolidated material at high temperature [Fig. 6(b)]. This effect is particularly severe in downward-facing surfaces because the solid material lies on a layer of loose powder that does not allow for effective heat dissipation [139]. Before complete solidification, the molten material may also partially penetrate into the powder bed due to gravity and capillarity effects, promoting dross formation [140]. In PBF-LB/M, supports are often added in the design to secure overhanging surfaces and improve heat dissipation. However, the removal of these sacrificial structures at the end of the printing process can be challenging, especially in small and intricate parts [141], and leave macroscopic marks, thus requiring significant postprocessing efforts to achieve a good quality in downward facing surfaces [142]. The top surface, on the other hand, may exhibit discontinuities caused by instabilities in the melt track due to improper selection of the laser scanning parameters. This phenomenon is known as balling [Fig. 6(c)] [143].

Proper calibration of the process parameters is also crucial for producing high-quality parts, with optimized characteristics for the specific application and minimal defect content. While the possibility to tune numerous settings with a certain degree of freedom allows for adjustments based on design specifications, understanding

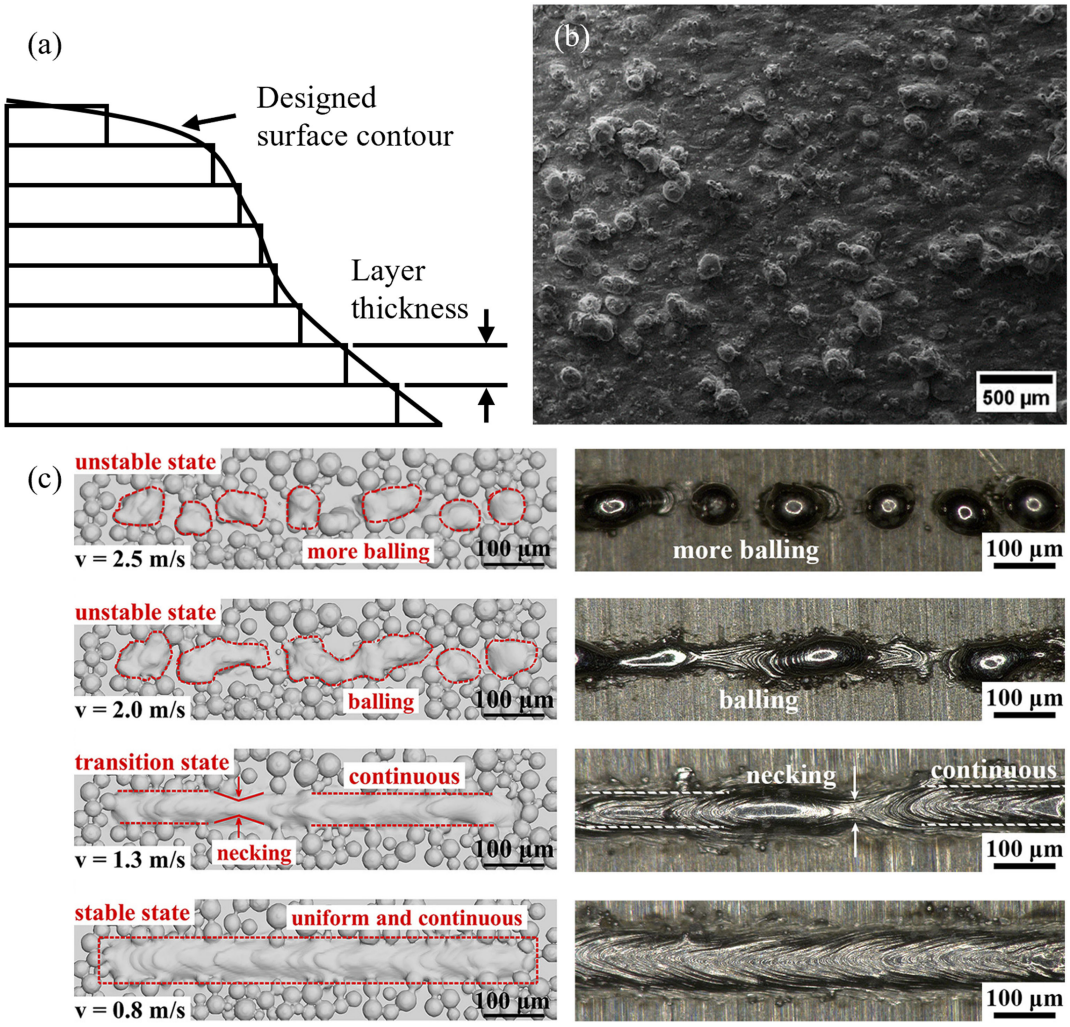

FIG. 6. (a) Schematic of staircase effect, (b) powder particles sticked on the lateral surface of as-built specimens made by PBF-LB/M [144], and (c) balling caused by instabilities in the melt track during PBF-LB/M [143].

the influence of each parameter and their combinations on the characteristics of the printed material is not always trivial. Ensuring a good reproducibility across various printing operations can also be challenging, as small variations in the process parameters and raw material quality can significantly alter the properties of the produced parts [12].

C. Operating conditions

In addition to standard procedures for evaluating material properties, such as mechanical strength and electrical conductivity, accelerator applications often demand specialized testing to ensure that components can withstand the extreme conditions they may encounter during service. Depending on the specific application, aspects like vacuum tightness and outgassing rate, material behavior at cryogenic temperatures, rf properties, high-voltage holding, and resistance to radiation damage may need a thorough examination.

In recent years, existing test facilities and protocols have been adapted for the qualification of additively manufactured components designed for UHV, rf, and high-voltage applications, taking into account the peculiar characteristics resulting from AM processes [145,146]. One major concern is represented by the typically large surface roughness of as-printed parts, which may significantly influence their performance, specifically in terms of outgassing rate, impedance, and breakdown strength.

1. Ultrahigh vacuum compatibility

The key parameters influencing the UHV compatibility of a component are the outgassing rate and the leak rate, which collectively determine the attainable ultimate pressure [147]. The typical surface roughness found in additively manufactured parts is often associated with relevant outgassing, driven by the high surface area promoting the adsorption of contaminants. The printing process may also produce small voids and channels in the material, causing

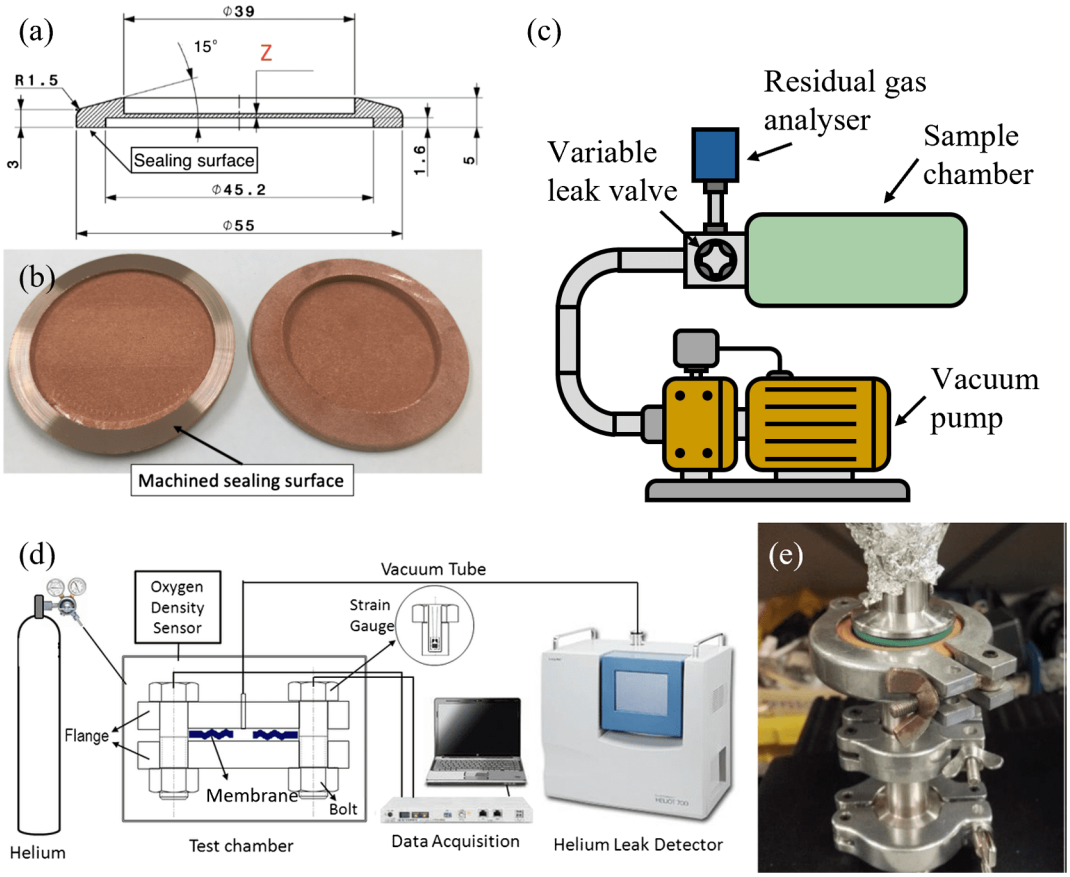

FIG. 7. (a) Design and (b) photograph of additively manufactured vacuum membranes [151], schematics of experimental setups for (c) outgassing and (d) helium leak testing [152], and (e) photograph of the clamped membrane during helium leak test [151].

significant leakage [148,149]. Therefore, specific testing is required to demonstrate UHV compatibility of materials processed with AM methods.

Dedicated setups are in use at CERN for the assessment of vacuum tightness and outgassing performance of ISO KF and CF-type test membranes [Figs. 7(a) and 7(b)]. During outgassing testing, the membrane is installed inside a vacuum chamber, and then the system is baked to remove water and closed using an adjustable valve [Fig. 7(c)]. Following an accumulation period, the valve is opened and the pressure is measured by a residual gas analyzer. The amount of released gas is calculated by integrating the pressure evolution and used to determine the outgassing rate [150]. The helium leak detection system is depicted in Fig. 7(d), with a test membrane clamped by an in-house designed tool [Fig. 7(e)]. During the test, the system is pumped down to its limit pressure and helium is sprayed on the upper surface of the test membrane. When helium passes through the membrane due to the presence of a leak, it is detected by a mass spectrometer. Since 2016, these experimental setups have been used for the characterization of membranes made by AM using different materials, technologies, thicknesses, and build orientations [146,151].

A similar apparatus was developed by Romanescu *et al.* [147] to assess the vacuum compatibility of additively manufactured thin plates. The outgassing rate is measured inside a T-shaped vacuum chamber connected to a vacuum gauge, while an experimental test stand based on the vacuum hood method is used to determine the leak rate. The specimens are sealed on a flange connected to a vacuum pump and equipped with a helium pipe at the bottom. The helium leak rate is determined using a mass spectrometer while pumping down the volume enclosed by the flange and the thin plate under testing. Additional residual gas analyses can also be conducted to quantify the level of surface contamination causing excessive outgassing.

2. *Radio-frequency performance*

The performance of rf components significantly depends on their surface quality, because the majority of the current is carried within the thin external layer known as the skin depth [153]. The surface roughness of parts produced by AM in as-built conditions (typically, 5–30 μm depending on the surface orientation relative to the build direction) is

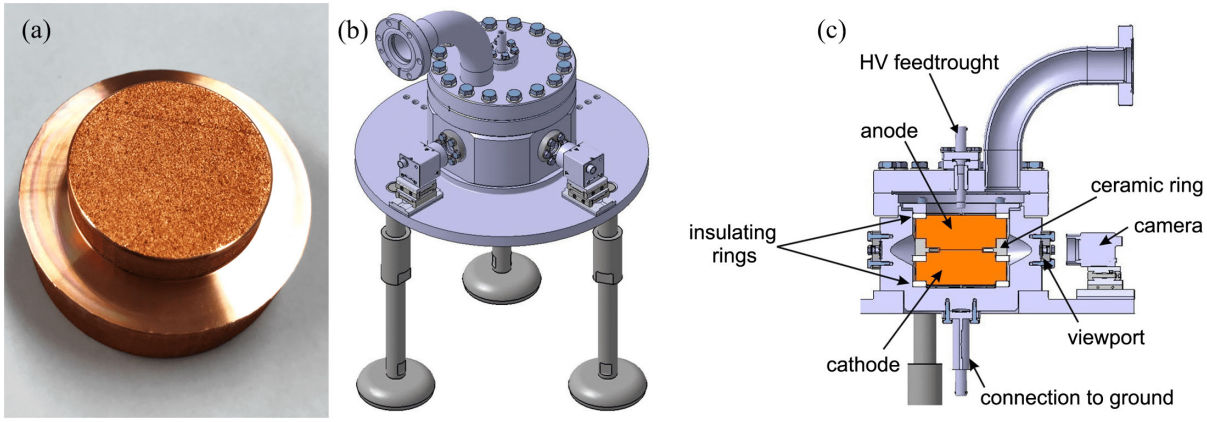

FIG. 8. (a) Photograph of a copper cathode made by PBF-LB/M for high-voltage testing and (b) schematic of pulsed high-voltage dc experimental setup with (c) cross-sectional view of the vacuum chamber [163].

much larger than the skin depth. This leads to increased surface resistance, usually associated with large ohmic power losses and poor rf properties [154]. Surface roughness also has a pronounced impact on the operating parameters of rf waveguides, such as attenuation and phase constant [155]. This makes the prediction of the behavior of additively manufactured parts during rf operation more complicated, due to the various interconnected phenomena affecting the surface quality of printed parts [23]. In response to these challenges, great efforts have been devoted in recent years to enhance the understanding and control of surface quality in additively manufactured components for rf applications, along with the development of advanced postprocessing techniques proving effective even with the typical geometric complexity of these parts [156–159].

3. High-voltage holding

The use of large accelerating potential gradients has been recognized as a key factor in pushing the energy scale in particle physics research and commissioning compact accelerator facilities for industrial and medical applications [123]. However, the achievable accelerating gradient is limited in practice by the occurrence of vacuum arc breakdown phenomena. Before commissioning, accelerating structures undergo conditioning, during which they are subjected to hundreds of millions of rf pulses with increasing power input. These pulses induce microstructural modifications that progressively enhance the breakdown strength of the material [123]. Extensive research has been conducted to understand the physical processes behind conditioning, aiming to reduce required run time and achieve higher voltage endurance. Investigations on the conditioning behavior of rough surfaces demonstrated that a higher surface roughness results in a lower initial breakdown voltage and a larger number of breakdown events necessary to complete conditioning [160,161].

Ongoing research is focused on determining how current knowledge can be extended to additively manufactured components that have a relatively large surface roughness in as-built conditions [162]. The pulsed high-voltage dc system installed at CERN is being used for high electric field testing of copper cathodes produced by PBF-LB/M [Fig. 8(a)] [162]. The experimental setup [Figs. 8(b) and 8(c)] consists of a UHV chamber housing two round flat electrodes separated by a ceramic spacer, which provides a well-controlled gap in between [163]. A pulsed generator is used to apply voltage pulses to the electrodes at a high repetition rate [123]. Breakdowns are detected from voltage and current signals recorded by an oscilloscope, which are combined with photographs of light emission events to determine the sequence of breakdown locations. These data are then correlated with postmortem microscopic analyses [163].

V. ADDITIVE MANUFACTURING APPLICATIONS IN PARTICLE ACCELERATORS

To the authors' knowledge, metal AM was first applied in the accelerator sector (or nuclear physics, in broader terms) in 2005 [164], using a hybrid process that combined LMD and milling. This method was employed to manufacture a conformal structure for the coil housing of the ARIES compact stellator [165]. Since then, the number of publications addressing AM-related topics in particle accelerators has steadily increased over the years. A clear indication of the growing interest within the accelerator community is given by the increasing number of contributions on AM presented in recent years at the IPAC conference series: 0 in 2019 and 2020, 3 in 2021 and 2022, and 12 in 2023. Table I in Supplemental Material [166] presents a comprehensive list of studies available from the open literature to the best of the authors' knowledge, providing information on the year of publication, application area, materials, and AM technologies used, along with references for further reading. Research has touched on several areas in the accelerator sector, including ion source and magnet components, rf cavities and waveguides,

beam intercepting devices, as well as vacuum and thermal management systems.

A. Ion source and magnet components

Ion and electron sources are used in accelerator facilities for scientific research, medical, and industrial applications to generate electrically charged particles that are focused and accelerated to produce high-energy beams [167,168]. In recent years, AM processes have been explored for the fabrication of ion source cathodes with a relatively complex design featuring connecting flanges and internal cooling channels. Frigola *et al.* [169] manufactured a prototype of the copper cathodes used in the UCLA Pegasus 1.6 cell photoinjector with PBF-EB, incorporating internal cooling channels in the cathode design for improved thermal management during operation (Fig. 9). Despite exhibiting a slightly lower electrical conductivity compared to conventionally machined OFE copper counterparts, the additively manufactured prototype demonstrated a comparable performance during rf testing, achieving a stable operation with 70 MV m^{-1} peak electric field after a 2-h conditioning and producing a 3.3 MeV photoelectron beam with a quantum efficiency of $\sim 2 \times 10^{-5}$.

Similarly, Girotto *et al.* [170] leveraged the design flexibility of PBF-LB/M to simplify the manufacturing process of the Isotope Separation On-Line (ISOL) ion source cathodes. In the standard production route, tantalum pieces are machined to shape the cathode body, flange, and outer cylinder, which are then welded together via a tungsten inert gas (TIG) operation [Fig. 10(a)]. Challenges associated with tantalum machining [171], along with possible postwelding distortions and residual stresses, often result in poor dimensional accuracy of the final component, introducing uncertainties in the performance and reliability of the ion source. PBF-LB/M, on the other hand, allowed monolithic prototypes to be fabricated in a single step, requiring only a slight modification of the cathode design to avoid any subtractive operation after printing [Fig. 10(b)]. The fabricated parts showed a deviation from the specified dimensions of less than 0.1 mm and maintained structural integrity during high-temperature testing at 1200 °C, indicating the absence of significant residual stresses.

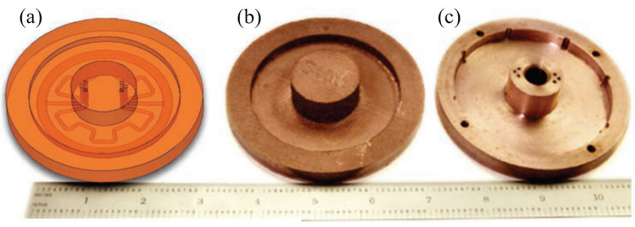

FIG. 9. (a) CAD model of UCLA Pegasus 1.6 cell photoinjector showing internal cooling channels and photographs of the cathode made by PBF-EB in (b) as-built conditions and (c) after final machining [169].

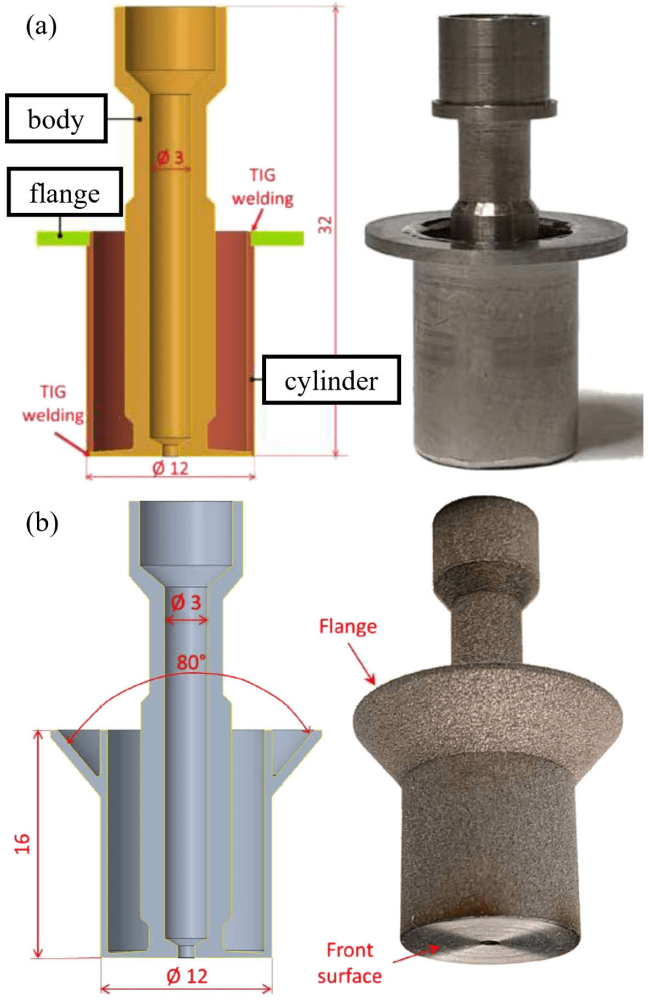

FIG. 10. ISOL ion source tantalum cathodes manufactured by (a) TIG welding of machined tantalum pieces and (b) PBF-LB/M [170].

Tantalum ion source cathodes were also the subject of a study that explored the potential of repairing Penning ionization gauge (PIG) ion source electrodes damaged during operation in a medical superconducting cyclotron [126]. Repair strategies based on LMD using high-purity tantalum feedstocks in both wire and powder form were developed to restore the damaged parts for reuse in the cyclotron (Fig. 11).

AM has also found application in the manufacturing of structural components for magnets used in high-energy accelerator facilities, such as the end spacers of 15 T dipole coils [Fig. 12(a)] [172,173]. In the framework of ARIES compact stellator development, Waganer *et al.* [165] designed a continuous convoluted toroidal support structure, made of low-carbon boron steel and equipped with grooves on the inner surface for housing the magnet coil windings [Fig. 12(b)]. The designed wall thickness of the tube was varied based on the local electromagnetic forces acting on it. Given the considerable complexity of the part,

FIG. 11. PIG ion source tantalum cathodes repaired by wire- and powder-based LMD [126].

the analysis of possible manufacturing methods revealed that LMD could reduce by two-thirds the production costs compared to forming and casting processes, as it avoided the fabrication and assembly of thousands of individual parts, which would have required substantial manual labor and carried a significant risk of mismatches.

Ferchow *et al.* [174] developed a strategy to optimize the PBF-LB/M fabrication process of a superconducting solenoid coil winder made of 316L stainless steel (Fig. 13). The orientation of the part during the printing process relative to the build platform was chosen to avoid highly inclined surfaces that would have required support structures difficult to remove in postprocessing steps. In addition, two distinct sets of process parameters were selected: one for manufacturing fully dense spars capable of withstanding the highest stresses during coil operation, and another for creating dimple-rich rib surfaces to enhance adhesion with the epoxy resin used to secure the coil cables in the winder channels. The use of a higher laser scan speed in areas where a relatively high porosity content was acceptable also reduced fabrication time and cost, demonstrating the advantages of a design approach based on local optimization of material characteristics in addition to component geometry.

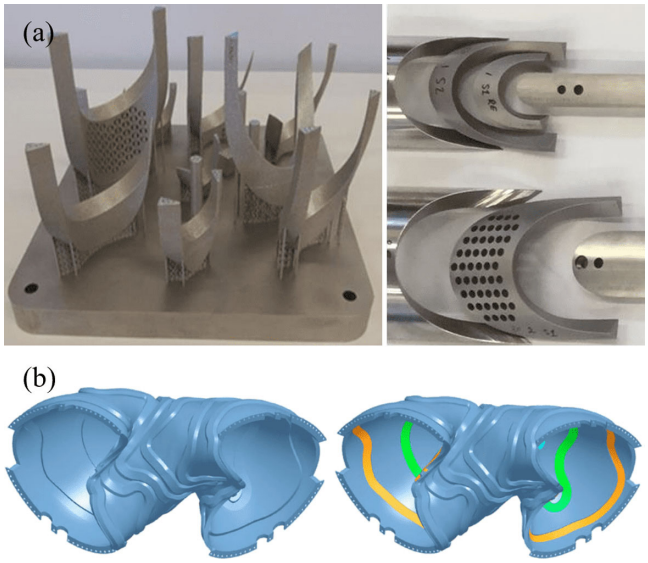

FIG. 12. (a) Additively manufactured titanium end spacers for MQXC coils [173] and (b) coil support structure of the ARIES compact stellator without and with coils in the internal grooves [165].

B. Accelerating structures

AM was first proposed by Frigola *et al.* [62] for the fabrication of accelerating structures in 2008. They successfully manufactured a pure copper 1.6 cell rf photoinjector with a 3 kW average power and 100 Hz repetition rate employing PBF-EB. The design featured a sophisticated cooling system, comprising six longitudinal channels and four channels surrounding the coupling iris region between successive cells [Figs. 14(a) and 14(b)]. The use of conformal channels with a star cross section [Fig. 14(c)] significantly improved the cooling efficiency compared to the conventional design with straight channels, preventing the formation of hot spots and reducing the cavity wall temperature by 25 °C during the operation of the rf gun.

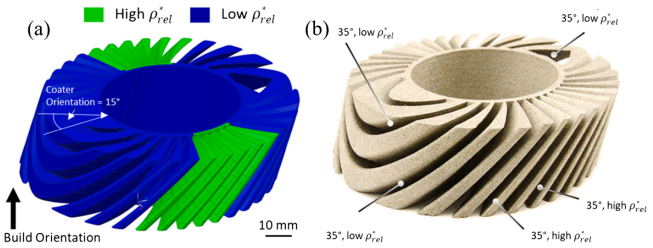

FIG. 13. (a) Design of the winding former optimized for PBF-LB/M, highlighting the high- and low-density regions manufactured with the two distinct sets of process parameters and (b) photograph of the printed part [174].

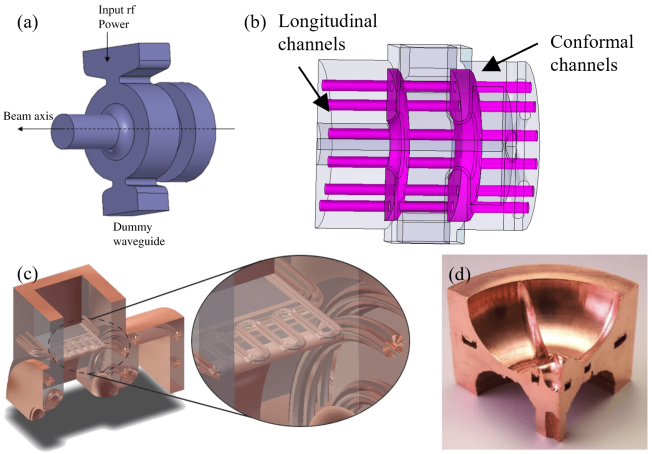

FIG. 14. (a) Design of the 1.6 cell rf photoinjector gun, (b) model of the internal cooling system, (c) CAD rendering of the gun highlighting the conformal cooling channels with star-shaped cross section, and (d) photographs of a quarter cell fabricated by PBF-EB [176,178].

The inner surface of the channels was intentionally left in as-built conditions to generate a turbulent flow, further improving heat transfer. Subsequent improvements were made to the photoinjector design to decrease the multipole components of the electromagnetic field inside the gun, affecting the beam brightness. In particular, an additional waveguide acting as a dummy load was used to lower the dipole field component, while the quadrupole mode was significantly reduced through a track geometry. The shape, thickness, and radius of the iris connecting the individual cells [Fig. 14(d)] were also optimized to minimize rf pulsed heating, mitigate distortions caused by thermal stresses, and reduce the electric field at the surface, effectively preventing the occurrence of breakdowns [175]. The improved version of the rf photoinjector could operate in the S-band with a repetition rate of 500 Hz [176]. This joint collaboration between RadiaBeam Technologies, UCLA, and INFN culminated in a patent filed in the United States for the manufacturing of rf cavities where "the wall of the conductive housing is made by a metal additive manufacturing technique in such a way as to produce a flow path that has a gentle trajectory without discontinuities in gradient" [177].

Other examples of rf cavity prototypes manufactured by AM can be found in the literature. Nantista *et al.* [179] developed a novel design for a string of rf cavities for a traveling wave tube amplifier to take full advantage of the PBF-EB process. Replacing the horizontal disk faces with conical surfaces allowed four strings to be printed vertically in a single job, resulting in a ∼50% reduction of manufacturing costs compared to the standard production process. PBF-EB design freedom was also harnessed by Frigola *et al.* [180] to integrate a 3D lattice structure in the design of single-cell 3.8 GHz SRF cavities made of pure niobium [Fig. 15(a)]. During operation, these cavities are often subjected to strong Lorentz forces, exerting outward pressure at the equator and inward pressure at the iris. The resulting local deformations can lead to the detuning of the cavity frequency, thereby limiting the achievable accelerating field [181]. While the conventional method of welding support rings onto cavities introduces additional complexity in the manufacturing process and may cause surface contamination, the integration of stiffening structures into the initial design becomes straightforward when following AM routes. AM also enables the design of devices with varying wall thickness, reinforced in areas exposed to higher stresses during operation, which cannot be easily produced with conventional manufacturing processes like deep drawing, spinning, and hydroforming [182]. These investigations led to the filing of a second U.S. patent for the manufacturing of "nearly monolithic SRF niobium cavities and end group components of arbitrary shape with features such as optimized wall thickness and integral stiffeners, greatly reducing the cost and technical variability of conventional cavity construction" [183].

INFN research group [14,184,185] also demonstrated the capability of PBF-LB/M of fabricating seamless 6 GHz SRF cavities, avoiding any welding operation that may lead to breakdown caused by inclusions [182] and ensuring a better reproducibility of the cavity performance. While copper cavities [Fig. 15(b)] were successfully

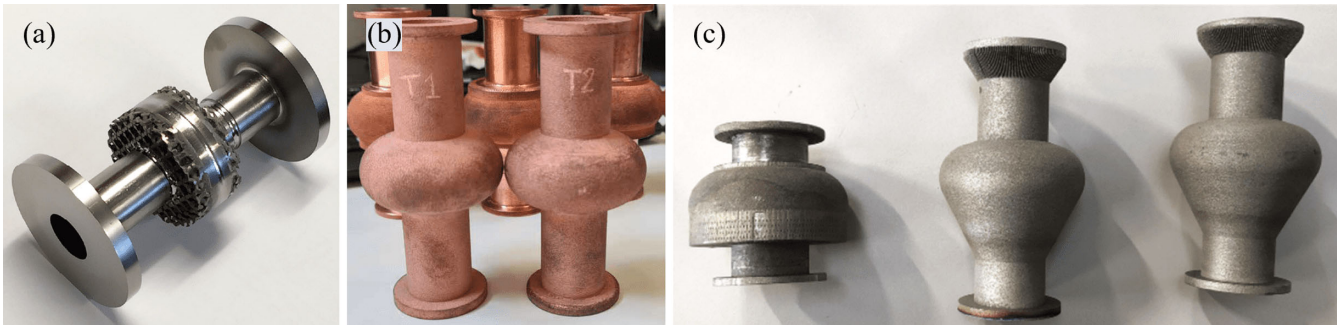

FIG. 15. (a) Single-cell 3.8 GHz niobium SRF cavity made by PBF-EB [180] and 6-GHz SRF cavities of (b) pure copper [184] and (c) pure niobium made by PBF-LB/M [185].

manufactured without any support [184], an innovative noncontact structure was integrated into the design of the niobium cavities [Fig. 15(c)] to act as a support for surfaces inclined by less than 35° relative to the build platform. The support structure followed the profile of the inner surface of the cavity's upper shell while remaining separated by a few layers of loose powder. The presence of this bulk structure improved the heat dissipation during the printing process, resulting in a lower roughness of down-skin regions of the cavities compared to nonsupported samples. Moreover, as it was not welded to the cavity's internal walls, it could be easily extracted from inside at the end of the printing process without the need for complex cutting operations. A novel PBF-LB/M approach was also adopted by Riensche *et al.* [186] to fabricate AlSi10Mg prototypes of rf quarter-wave cavity resonators (QWRs). They employed a commercial hybrid PBF-LB/M machine integrating a vertical three-axis milling tool for *in situ* machining of specific features, critical for the rf performance of QRWs, including the outer conductor, central pin, shorting plane, and service surfaces. A milling operation was performed after every ten layers of deposition, corresponding to a thickness of ∼0.5 mm. Thanks to their superior surface finish, the QRWs manufactured with the hybrid process exhibited a significantly higher and more stable Q-factor compared to their counterparts made by standard PBF-LB/M, as well as a resonant frequency closer to the ideal value. Another aluminum alloy, the Al12Si grade, was employed by Creedon *et al.* [187] to manufacture superconducting microwave cavities by PBF-LB/M [Fig. 16(a)]. Si-containing aluminum alloys are well suited for the PBF-LB/M process because the high silicon content promotes the formation of a eutectic phase with a narrow solidification range and higher fluidity in the molten state, thus preventing hot cracking during solidification [188,189], resulting in excellent laser processability. Subsequent annealing of the printed device at ∼600 °C for 4 h significantly improved the Q-factor from 1.6×10^6 to 3.8×10^6, as the high temperature promoted the diffusion of silicon out of the supersaturated solid solution, leaving behind a purer aluminum matrix with higher electrical conductivity. A superconducting microwave cavity was also manufactured by Holland *et al.* [190]. They developed a novel design for a conical resonator and printed it by PBF-LB/M in a monolithic piece employing a Ti6Al4V powder [Fig. 16(b)]. The measured resonance of the device ($\omega_0/2\pi = 7.50$ GHz) was in good agreement with the simulated data.

PBF-LB/M has also been used to manufacture normal-conducting linear accelerator (linac) structures. Mayerhofer *et al.* [154] prototyped a five-cell drift tube linac (DTL) comprising four drift tubes and a network of cooling channels running through the cavity (Fig. 17). In the standard DTL design, each drift tube is supported by two stems to ensure stability during the brazing operations. However, the one-stem geometry allowed by PBF-LB/M results in a lower electromagnetic field interference, increasing the predicted shunt impedance by ∼18% compared to the two-stem configuration. They also slightly modified the shape of the upper region of the cavity and cooling channels to eliminate significant overhanging features and facilitate the printing of the DTL without the need for additional support structures. The additively manufactured DTL exhibited a ∼15% lower unloaded Q-factor and ∼4% lower shunt impedance compared to its conventionally produced counterpart. This was primarily attributed to the larger surface roughness, causing higher ohmic rf power losses at the cavity walls and promoting the occurrence of breakdown phenomena. A comparable performance was achieved after improving the surface quality by means of a commercially available chemical-electrochemical process [191]. Moreover, the production costs were reduced to one-third of those of the reference cavity.

A similar strategy was adopted to prototype biperiodic side-coupled linac structures, highlighting the potential of PBF-LB/M in manufacturing each cell with optimal length in terms of particle energy without additional cost or effort (Fig. 18) [9]. On the other hand, this approach is impractical with conventional methods, as the fabrication of several individual parts with dissimilar geometries would be economically unsustainable.

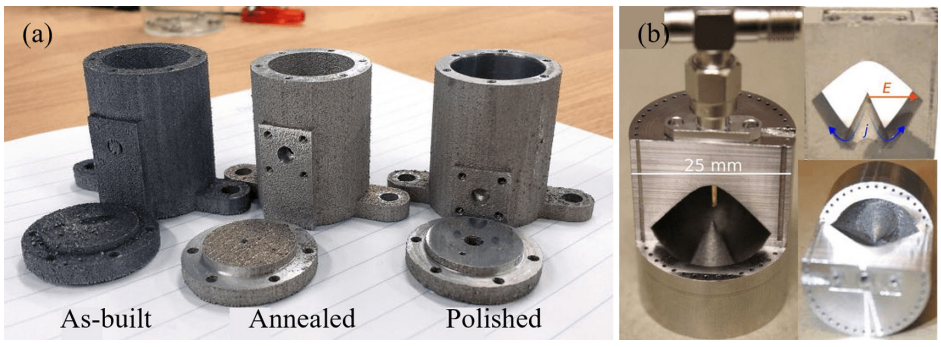

FIG. 16. (a) Additively manufactured Al12Si superconducting cavities in as-built condition, after annealing and machining, and in annealed and polished condition [187], and (b) Ti-6Al-4V conical resonator made by PBF-LB/M [190].

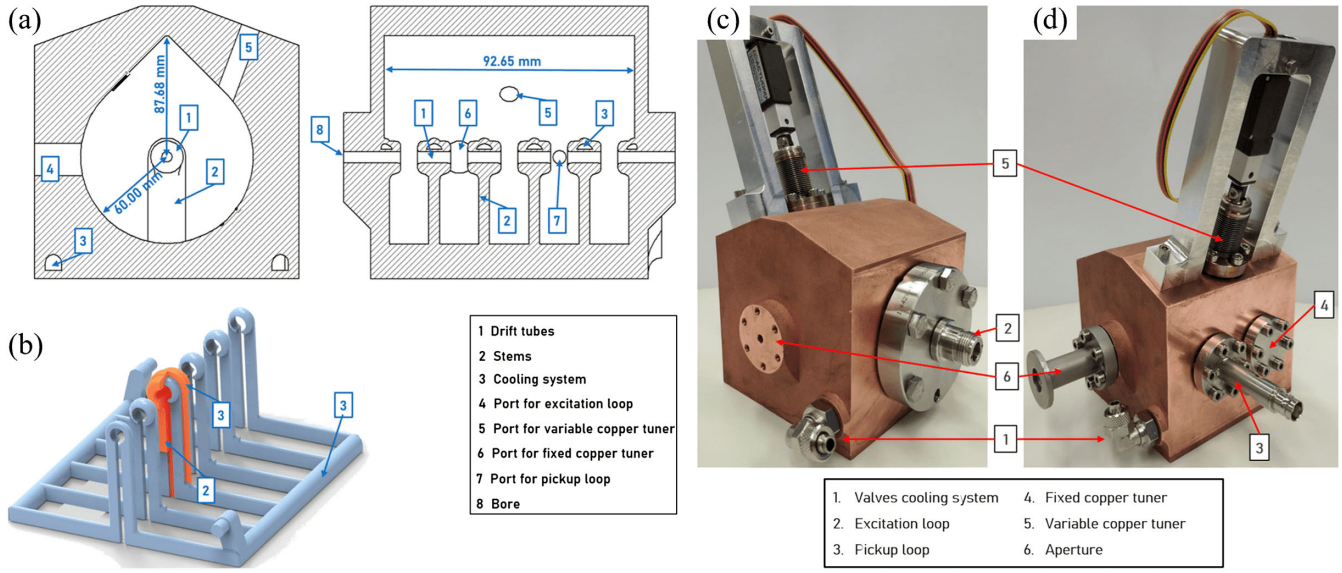

FIG. 17. Design of (a) DTL cavity and (b) cooling system and (c) front and (d) rear view of the fully equipped prototype [154].

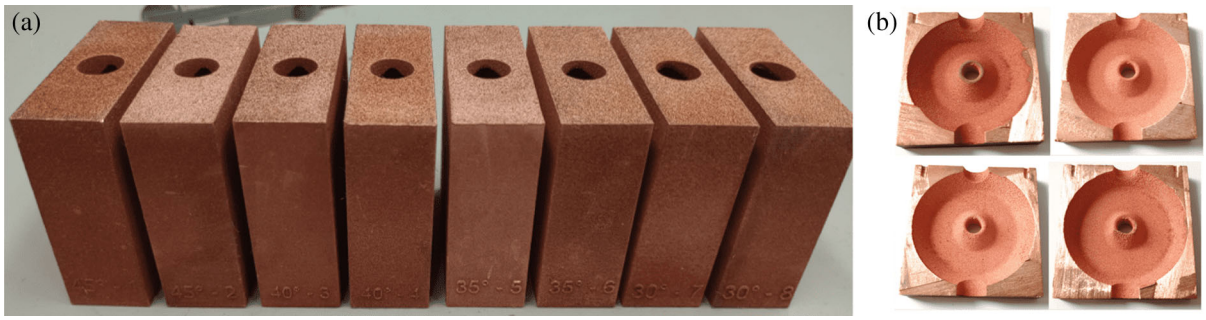

FIG. 18. (a) Additively manufactured side-coupled linac structures and (b) half-cells after cutting [9].

The economic advantage and ease of production of AM were also emphasized by Wehner *et al.* [192,193] who exploited the flexibility of PBF-LB/M to manufacture a complex klystron circuit with multiple rf cavities in only two parts with well-aligned matching features, which were subsequently brazed in a hydrogen furnace [Figs. 19(a) and 19(b)]. This approach provided significant benefits over the conventional fabrication process, which involves numerous intermediate machining and brazing operations, carrying the risk of vacuum and water leakage due to minor misalignments. The assembled circuit displayed no indication of leakage during the helium leak test, nor significant outgassing when placed in vacuum. The rf cavities, on the other hand, showed a substantial deviation in resonant frequency compared to the intended design. Further experiments conducted on test cavities with the same geometry as cavity 2 of the full klystron circuit [Fig. 19(c)] revealed a lower Q-factor and higher frequency than simulated values [Figs. 19(d) and 19(e)]. This was primarily attributed to the surface roughness of as-built cavity walls and inaccuracies of the PBF-LB/M process in reproducing the 3D model geometry.

In a series of publications, Hähnel *et al.* [194–198] demonstrated the manufacturing of 316L stainless steel and pure copper Interdigital H-mode (IH) DTL structures using PBF-LB/M. The 316L cavity was equipped with CF40 flanges for vacuum testing and rf coupler and tuner for low-level rf measurements. The structure also included cooling channels extending to the stems of the additively manufactured drift tubes [Fig. 20(a)]. An ultimate pressure of $\sim 10^{-7}$ was reached during vacuum tests after approximately 120 h pumpdown while the measured operating frequency and Q-factor showed good agreement with the expected values [198]. An improved design with smoothed surfaces was also developed to facilitate postprocessing operations, such as surface finishing and copper plating, and reduce the peak field for the benefit of high-power rf operation [Fig. 20(b)] [196]. The pure copper specimens [Fig. 20(c)], on the other hand, exhibited a lower Q-factor than expected. This was attributed to the peculiar microstructure resulting from the PBF-LB/M process, affecting the electrical conductivity of the material. Although the ideal value was not achieved, an improvement in the Q-factor of

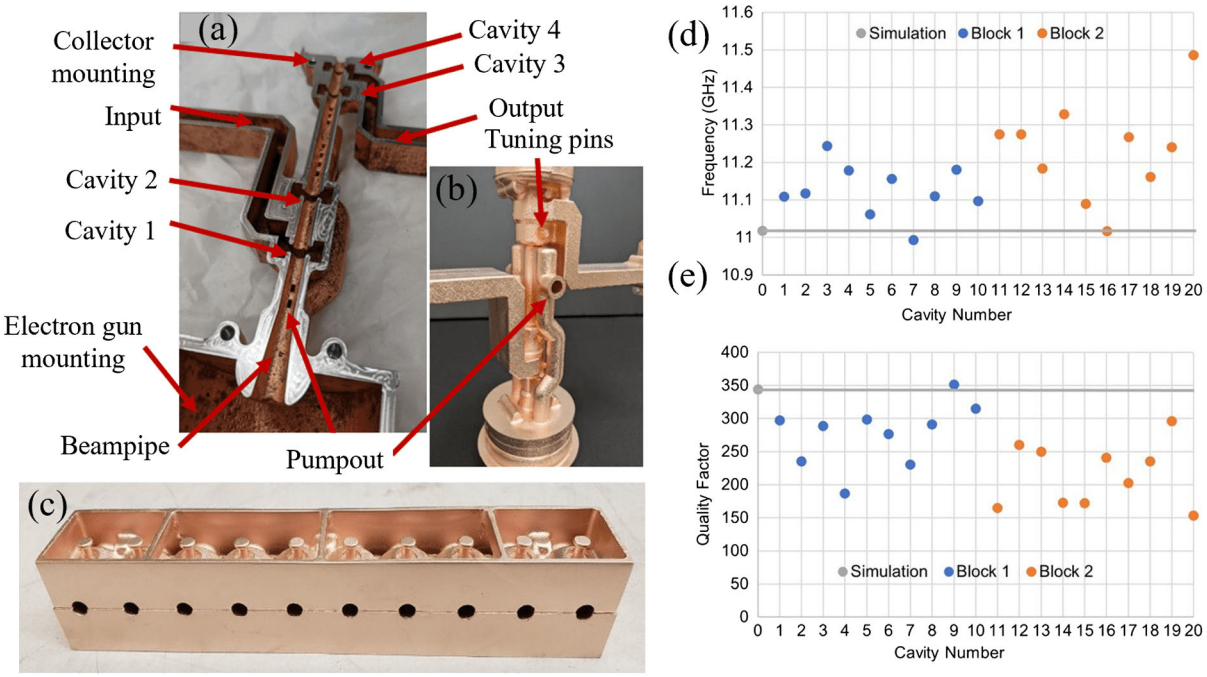

FIG. 19. Photographs of the (a) additively manufactured klystron circuit half-piece, (b) full circuit after brazing operation, (c) test cavities, (d) frequency, and (e) Q-factor measured on test cavities compared to simulated values [193].

FIG. 20. Additively manufactured IH-type DTL drift tube structure made of (a),(b) 316L stainless steel and (c) pure copper [194,195].

~18% was observed after annealing the parts at 300–400 °C for 1 h to induce recrystallization.

Another core element of many linac facilities, the radio-frequency quadrupole (RFQ), was prototyped by Torims *et al.* [13,199] using a commercial PBF-LB/M machine equipped with a high-power green laser source to process an electrolytic tough-pitch pure copper powder. In the first iteration, they printed one-quarter of a 750 MHz RFQ [Fig. 21(a)] [13]. The implementation of topologically optimized cooling channels and internal honeycomb structure replacing the massive walls of the standard design led to a weight reduction of ~37%, also resulting in significant material saving and reduction of printing time. The required geometrical accuracy of 20 μm was successfully achieved for the vane tip. Subsequently, a four-vane RFQ demonstrator of 250 mm length and 148 mm cross-section diameter was manufactured in a single piece, without the need for complex and time-consuming brazing operations [Fig. 21(b)]. This improved design included flanges and orifices for vacuum and rf testing, respectively [199]. A larger version of 400 mm in length was showcased at the Formnext exhibition in 2022 [Fig. 21(c)] [200].

The research on AM of rf devices led to the filing of a European patent describing a "method of manufacturing a radio-frequency cavity resonator having a tubular structure extending along a longitudinal axis and a plurality of tubular elements, in particular drift tubes, arranged within the tubular structure, […], that is more cost efficient than the manufacture according to prior art" [201]. PBF-LB/M of copper and copper alloys is also being investigated for the production of acceleration grids for nuclear fusion reactors [202,203].

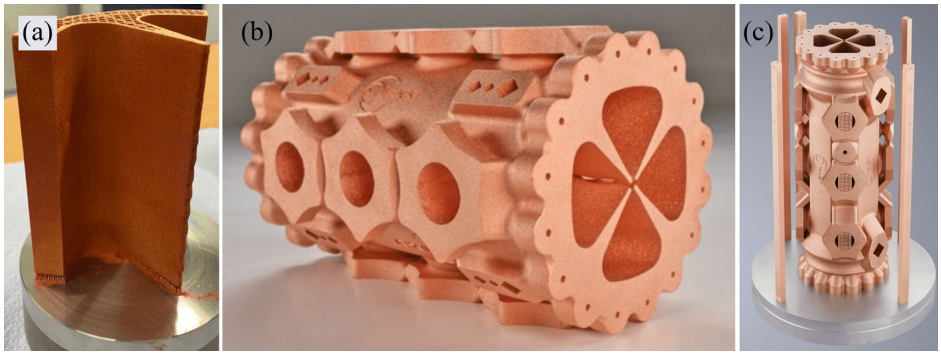

FIG. 21. Photographs of (a) one-quarter [13], (b) 250 mm long [199], and (c) 400 mm long four-vane RFQ prototypes made by PBF-LB/M [200].

C. Radio-frequency waveguides and loads

rf waveguides are structures designed to guide and manipulate electromagnetic waves, playing a crucial role in accelerator facilities by delivering the rf power from external sources, such as klystrons and magnetrons, to rf cavities for the acceleration of charged particles [204]. While conventional waveguides are established components in rf systems, ongoing research is exploring innovative designs to enhance their functionality [205], for example, for the delivery of THz radiation to high-field gradient accelerator and beam manipulation facilities [155,206]. However, the manufacturing of such devices poses challenges for conventional fabrication methods due to their geometrical complexity and small feature size (on the mm scale), resulting in high production costs and limited design flexibility. Hence the growing interest in recent years in AM applied to the fabrication of waveguides and other rf components.

The first additively manufactured prototypes of an rf waveguide were showcased by Grudiev [207] during the CLIC14 workshop. 20 cm long Ti6Al4V WR90 waveguides were produced using PBF-LB/M and PBF-EB technologies. Extensive testing of printed samples involved the characterization of shape accuracy, surface roughness, microstructure and mechanical properties, dc conductivity, rf loss, leak tightness, and outgassing rate. Further development led to the manufacturing and testing of an improved design, featuring an additional cooling jacket, increased wall thickness, and vacuum flange implementation (Fig. 22) [208]. A prototype made of 316L stainless steel was also fabricated by PBF-LB/M. The outputs of the experimental campaign suggested that the PBF-EB technology was not as mature as the laser-based process. Moreover, issues regarding surface roughness and geometrical tolerances were identified as the next challenges to face for part validation.

A similar conclusion was drawn by Kellermeier *et al.* [155], who fabricated 316L stainless steel horn waveguides using PBF-LB/M [Fig. 23(a)]. As expected, dispersion measurements showed that the phase velocity of the printed devices decreased with increasing the nominal inner radius from 0.75 to 0.95 mm [Fig. 23(b)]. However, microscopic inspection revealed a systematic deviation of ~0.07 mm in the effective radius. This shift caused the waveguides to be inherently overmoded, exhibiting wiggles explainable by multimode excitation.

Various types of waveguides made of pure copper were also manufactured using PBF-EB. Horn *et al.* [210] produced a WR10 waveguide and polished it employing magnetically driven abrasive media. rf testing results

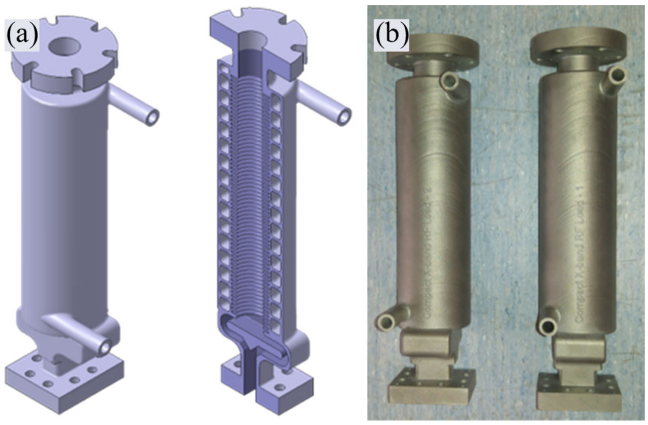

FIG. 22. (a) CAD model and (b) photograph of additively manufactured Ti6Al4V WR90 waveguides [209].

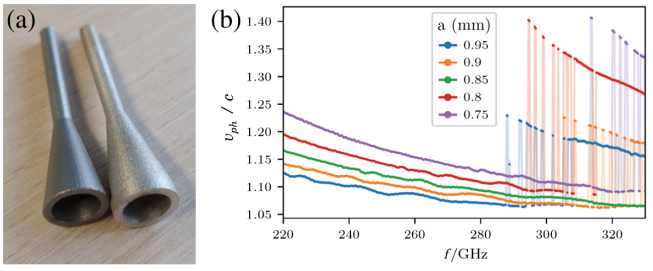

FIG. 23. (a) Photograph of additively manufactured horn waveguides and (b) measured dispersion of printed waveguides with varying inner radius [155].

indicated comparable losses (0.8 dB cm^{-1}) to conventionally produced reference parts. In another study, Lomakin *et al.* [205] fabricated two WR12 waveguides using different electron beam scan strategies to evaluate their effect on the performance of the printed devices. In the first approach, they rotated the scan direction by 90° between layers, while the second approach involved creating a contour around the region already processed with the electron beam in each deposited layer. Since both specimens were printed vertically (i.e., with the build direction parallel to the wave propagation direction), the same wavy pattern caused by the layer-wise fabrication was observed on their outer surface. However, the part manufactured with the first strategy also exhibited marked grooves at cross-sectional edges, resulting in a significantly higher attenuation compared to the reference waveguide. On the other hand, the contour strategy produced even cross-sectional edges, leading to an attenuation coefficient closer to the ideal value.

Lanza *et al.* [211] also conducted helium leak and outgassing tests on copper X-band waveguides made by PBF-EB to demonstrate their suitability for implementation in UHV systems. Following printing, the parts were annealed at 900 °C in UHV to reduce the oxygen content to 20 ppm. During leakage testing, the waveguides were successfully pumped down to a pressure lower than 10^{-4} Torr, displaying a helium background of 4×10^{-9} Torr $l\,s^{-1}$. Outgassing measurements conducted after baking the specimens at 250 °C for 48 h did not reveal any significant outgassing, indicating an outgassing rate below that of the testing chamber walls.

A significant impetus for the research on AM for the production of rf components stemmed from CERN's investment in the Compact Linear Collider (CLIC), which demanded the development of compact devices capable of operating at more than 50 MW peak power and few kW average power to minimize the machine footprint [209,212,213]. Within this framework, Grudiev *et al.* published various reports showcasing the results progressively achieved in designing and manufacturing a novel X-band rf spiral load [Fig. 24(a)] [208,214,215]. This load was devised for implementation in the CLIC facility, aiming to absorb residual rf power not used for beam acceleration nor dissipated in the module walls [213]. The innovative concept behind this design was to make a long taper waveguide more compact by wrapping it inwards. Conveniently positioned holes on the load walls allowed the main vacuum pump placed at the center of the spiral to effectively communicate with the whole internal volume [Fig. 24(b)] [204]. A water cooling system was also integrated into the design [209]. The first load prototype, manufactured in 316L stainless steel via PBF-LB/M, exhibited high reflection during low-power rf testing, due to traces of contaminants on the internal surfaces. A second load, made of Ti6Al4V alloy [Fig. 24(c)], was successfully tested in the high-capacity X-band facility Xbox3 with up to 35.5 MW peak power for 50 ns pulses and 25 MW peak power for 200 ns pulses, at a repetition rate of 200 Hz [209].

Following the validation of the spiral rf load and registration under the terms of CERN's open hardware license [209], Bursali *et al.* [213] developed an improved design to facilitate the fabrication of multiple parts in a single print run. In the standard design, only one load can be manufactured in each cycle, as the part is constructed with an orientation of 45° relative to the build direction to avoid horizontal surfaces that would compromise quality. This orientation requires substantial support structures [Fig. 25(a)] that need to be removed at the end of the printing process, thereby increasing production costs and generating a large amount of waste material. An iterative optimization process, involving mechanical modeling and electromagnetic simulations, resulted in a new design that can be manufactured horizontally [Fig. 25(b)], allowing the stacking of several units within the powder bed. This can potentially reduce the cost per unit and enable faster manufacturing for mass production.

A spiral design was also developed by Mathesen *et al.* [206] for the rf loads of the Cool Copper Collider (C^3), a compact TeV accelerator planned to operate in the C-band frequency of 5.712 GHz to produce Higgs bosons. A load prototype was manufactured in two halves using PBF-LB/M to eliminate the need for internal support and ease the removal of excess powder at the end of the process. The printed parts were then welded together, and vacuum

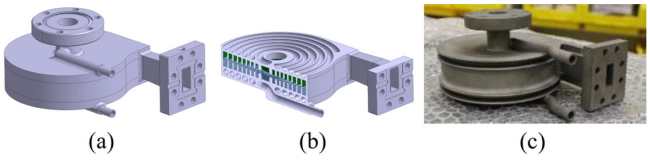

FIG. 24. (a) CAD model, (b) cross section showing the spiralized waveguide and vacuum pumping holes, and (c) photograph of additively manufactured spiral rf load [209].

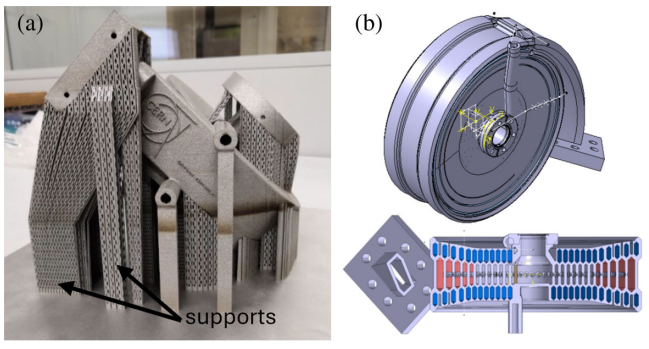

FIG. 25. (a) Photograph of additively manufactured spiral rf showing the supports and (b) CAD model of the novel design developed for mass production [213].

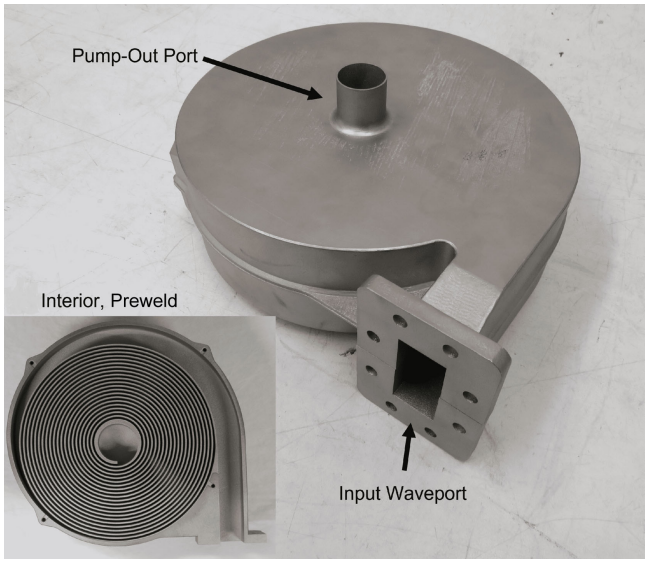

FIG. 26. Additively manufactured spiral rf load, with the inner structure shown in the inset [206].

pump port was added (Fig. 26). Preliminary cold tests conducted before and after welding operations displayed an increase in the S_{11} value from −38.7 dB to −25.1. The load underwent initial conditioning with 200 ns pulses up to 8 MW power and 20 Hz repetition rate. The pulse width was then increased up to 700 ns during high-power testing, demonstrating the load's capability to terminate a peak power of 8.1 MW. However, further testing with 1000 ns pulses could not be completed due to significant heating of the outer turns of the spiral and loss of vacuum pressure. Future design improvements include the integration of cooling channels and the optimization of waveguide geometry to enhance heat dissipation and prevent local loss concentrations.

D. Beam instrumentation and diagnostics

In recent years, AM has been used to manufacture prototypes and functional instruments employed in the management and characterization of particle beams in accelerators. In 2012, Veness *et al.* [216] suggested integrating AM in the fabrication route of advanced wire scanners to be installed in the pre-injectors of the LHC, aiming for high scanning speeds while providing high position and time accuracy [217]. They devised a novel design for the wire-supporting forks, considering stiffness requirements to keep the wire under tension and minimize vibrations during motion across the beam. Topological optimization of the fork geometry was also conducted to minimize its mass, thus reducing the inertial load on the motor during wire acceleration and deceleration phases [Figs. 27(a) and 27(b)]. The first prototype, printed in Ti6Al4V alloy using PBF-LB/M and postprocessed to machine precision details [Figs. 27(c) and 27(d)], was installed in the Super Proton Synchrotron (SPS) ring in

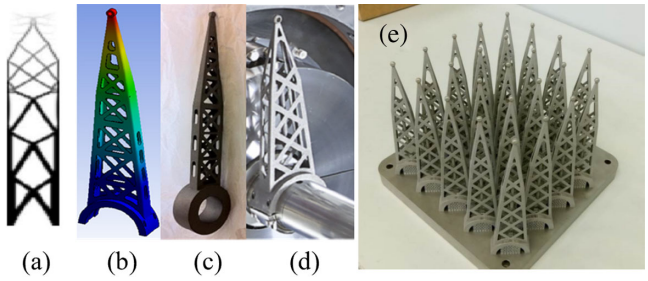

FIG. 27. (a) Topological optimization, (b) finite element analysis, (c) as-built, and (d) postprocessed wire scanner forks made by PBF-LB/M [218], and (e) series of printed forks with different geometries [219].

2015 [218]. Over the following 2 years, slightly different designs were developed to produce wire-supporting forks for the proton synchrotron booster (PSB) and the proton synchrotron, each tailored to the specific aperture of the machine [219]. The cost of each printed fork [Fig. 27(e)] was ∼35% of the conventionally manufactured counterpart.

The economic advantages associated with AM were also emphasized by Jenzer *et al.* [220] in the production of a stripline beam position monitor (BPM). The standard manufacturing routes typically involve welding together four different parts. However, the subsequent machining of the thin cylindrical striplines [Fig. 28(a)] poses significant challenges. On the other hand, thin-walled devices were readily fabricated by PBF-LB/M using a 316L stainless steel powder. The shape of the flange was topologically optimized to allow the fabrication of the BPM in a single print cycle without the need for support structures (Figs. 28(b)–28(d)). Since no additional space was needed for welding the flanges onto the BPM body, the part length could be reduced by 20 mm [Figs. 28(a) and 28(b)], resulting in a weight reduction of ∼40% compared to the original design. The design improvements enabled by the flexibility of PBF-LB/M process approximately halved the production costs and reduced lead times by a factor of 3. Following preliminary Lambertson and stretched wire tests, which demonstrated performance comparable to the reference component, a triplet comprising of two conventionally manufactured BPM and the additively manufactured BPM in between was installed in the PHIL (Photo-Injecteur au LAL) accelerator beam line [Fig. 28(e)]. All BPMs exhibited similar accuracy in position measurements during tests with 3.5 MeV beam energy [221].

PBF-LB/M was also employed by Grazzi *et al.* [222] to produce the exit snout of the MACHINA (Movable Accelerator for Cultural Heritage In-situ Non-destructive Analysis) transportable particle accelerator, which was installed on the beamline to extract the beam into the atmosphere. The exit snout design comprised two hollow focusing elements with a conical shape intersecting at the extraction window, as shown in Fig. 29.

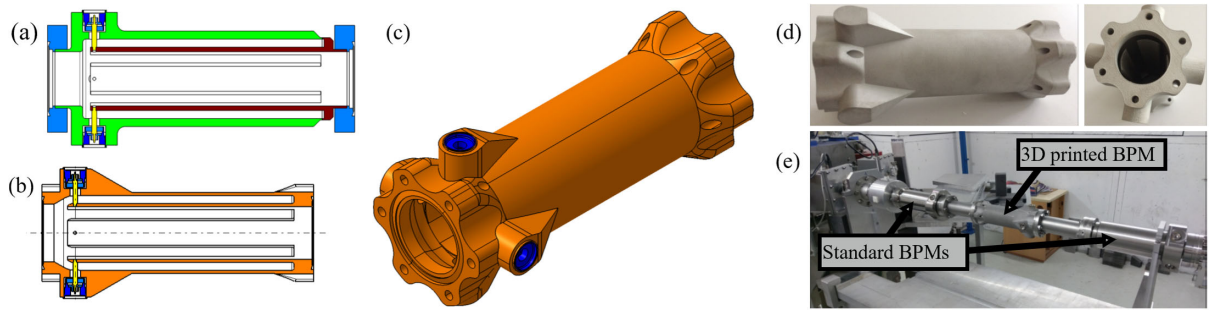

FIG. 28. Drawings of the (a) standard BPM and (b) topologically optimized design with (c) 3D CAD model, (d) photograph of BPM prototype made by PBF-LB/M [220], and (e) BPM triplet installed in PHIL accelerator [221].

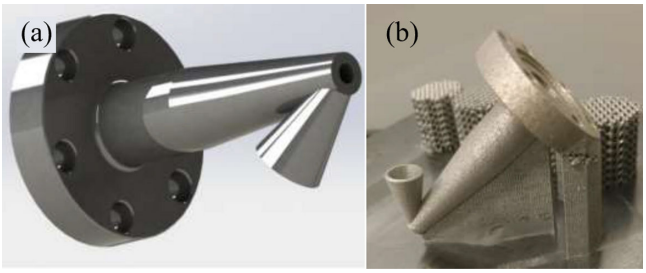

FIG. 29. (a) CAD model and (b) photograph of the additively manufactured beam exit snout of the MACHINA transportable accelerator [222].

As part of the SOLEIL synchrotron upgrade program, Tavakoli *et al.* additively manufactured compact crotch absorbers in CuCr1Zr alloy to be inserted downstream of the dipoles [Fig. 30(a)] [223]. Cooling channel optimization allowed reducing the maximum temperature by more than 30 °C compared to the conventional absorber design. In another study, Sinico *et al.* [224] prototyped a copper beam dump using PBF-LB/M. The device served to stop the proton beam at the end of a cyclotron beamline and dissipate the generated heat. It comprised a bulky disc with one face to be exposed to the beam and the other accommodating a cooling system. The cooling system, featuring a spiral geometry for water circulation, was printed using a pure copper powder on a build platform also made of copper, which served as the beam dump front [Figs. 30(b) and 30(c)]. A spiral channel configuration was also integrated into the PROTAD targets for antiproton production developed within the RaDIATE collaboration at CERN [225,226]. These targets consisted of a Ta/Ir core embedded in a matrix of expanded graphite and encapsulated in a double wall assembly with an internal spiral channel for compressed air cooling, which was manufactured by PBF-LB/M using a Ti6Al4V powder. Chan *et al.* [227] adopted a similar approach to develop a compact target holder design for the IBA Cyclone® 18/18 cyclotron, incorporating an internal cooling system for water circulation [Figs. 30(d) and 30(e)]. The sterling silver prototype fabricated by PBF-LB/M exhibited ~60% higher cooling

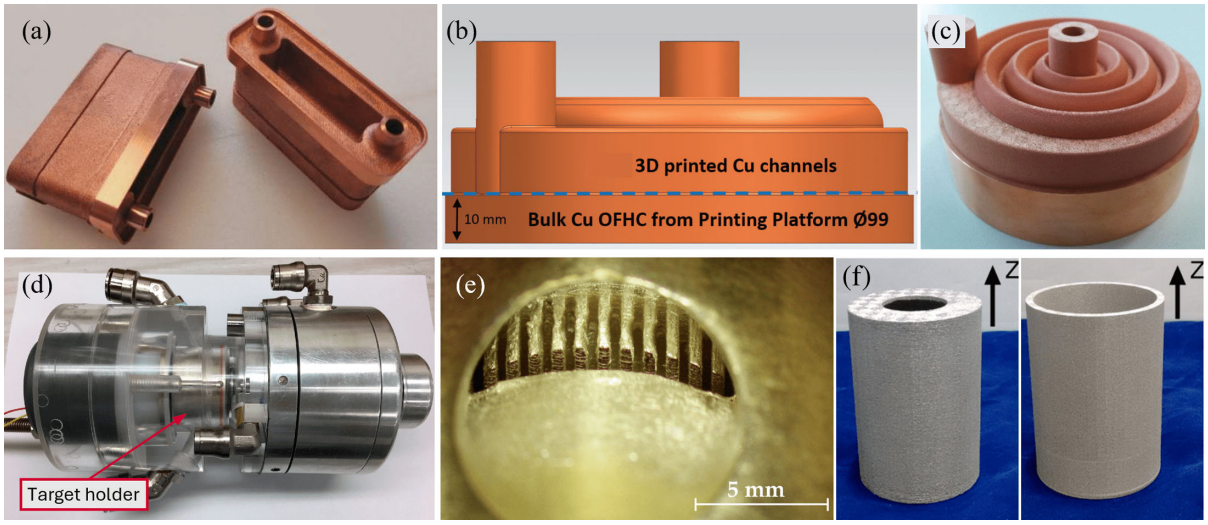

FIG. 30. (a) Additively manufactured crotch absorbers, (b) CAD design and (c) photograph of copper beam dump made by PBF-LB/M [224], (d) photograph of target assembly of the IBA Cyclone® 18/18 cyclotron with (e) detail of the internal cooling system of the additively manufactured target holder [227], and (f) cylindrical magnetic shielding structures made by PBF-LB/M [149].

efficiency compared to the standard target system, thereby enabling higher target currents. Additionally, the novel design allowed moving the target material closer to the exit port of the cyclotron, significantly reducing the beam losses caused by divergence.

PBF-LB/M was also employed by Vovrosh *et al.* [149] to fabricate cylindrical magnetic shielding components with a compact and lightweight design that could be tailored to the specific structure to be shielded [Fig. 30(f)]. The as-printed permalloy samples exhibited a preferential grain orientation along the Ni hard axis [100] resulting from the layer-wise fabrication, which negatively impacted the shielding properties of the material. HIP and annealing treatments mitigated this microstructural anisotropy, increasing the shielding factors (ratio between nonshielded magnetic field amplitude and residual field amplitude after field installation) to ∼150 and ∼260, respectively.

E. Vacuum devices

A variety of components is employed in particle accelerator facilities to provide the UHV environment required for their operation. These include, for example, gates, valves, seals, pumps, and other equipment essential for achieving and maintaining low-pressure levels [147]. Vacuum devices are often custom-made and produced in limited batches, employing sophisticated routes that involve multipart assembly operations and often result in high manufacturing costs. AM's inherent ability to create complex monolithic structures can help overcome these challenges [147].

Vovrosh *et al.* [149] demonstrated the possibility of using PBF-LB/M to manufacture UHV components made of Ti6Al4V alloy. They fabricated a test piece with a top hat profile and sealed it to a DN40CF flange using an indium wire [Figs. 31(a) and 31(b)]. The assembly was installed in an ion pump with triode configuration, with an additional reference branch equipped with a standard flange for comparison purposes [Fig. 31(c)], and the setup was baked out at 130 °C for 160 h. An ultimate pressure of 5×10^{-10} mbar was achieved at both the test and reference branches, with an outgassing rate of $\sim 4 \times 10^{-12}$ mbar l s^{-1} cm^{-2}. It should be noted that the contact surface of the additively manufactured flange was milled before the indium sealing operation, while the inner walls were left in as-built conditions.

This aligns with findings from other researchers, confirming that machining the inner surfaces of additively manufactured components is not strictly required to ensure vacuum tightness. Jenzer *et al.* [228] reported that 316L stainless steel DN40KF tubes made by PBF-LB/M [Fig. 32(a)] displayed a vacuum performance comparable with commercial products once machining the knife-edge seals, but leaving the internal walls unaltered. In another study, Cooper *et al.* [148] manufactured an AlSi10Mg vacuum chamber by PBF-LB/M [Fig. 32(b)] and tested it in a UHV setup [Fig. 32(c)] without further machining operations, except at the mating surfaces between the printed chamber and the components of the experimental apparatus. The chamber design comprised multiple conflat flange ports and integrated a gyroid lattice on the external surface to enhance the stiffness of the thin walls. Following a 120 °C bakeout of 120 h, the assembly was pumped down using a NEG combination ion pump, achieving an ultimate pressure of $\sim 10^{-10}$ mbar and maintaining it for more than 2 h without active pumping. Because of the high system complexity, a precise outgassing rate could not be determined, but its upper limit was estimated to be $\sim 10^{-13}$ mbar l s^{-1} mm^{-2}. Results from spectrometry and spectroscopy analyses attributed the good outgassing performance to the formation of a Mg-rich oxide layer on the material surface, capable of withstanding temperatures up to 350 °C and reducing the release of volatile species.

An additively manufactured vacuum chamber was also showcased by Wolf *et al.* [229], who integrated a system of

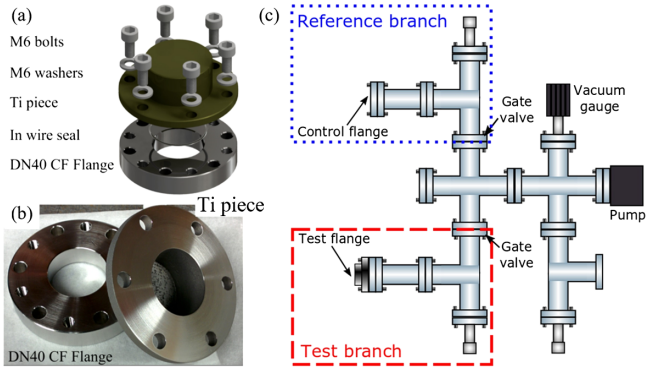

FIG. 31. (a) 3D model and (b) photograph of vacuum flange assembly with additively manufactured Ti6Al4V test piece and (c) schematic diagram of the experimental setup for vacuum testing [149].

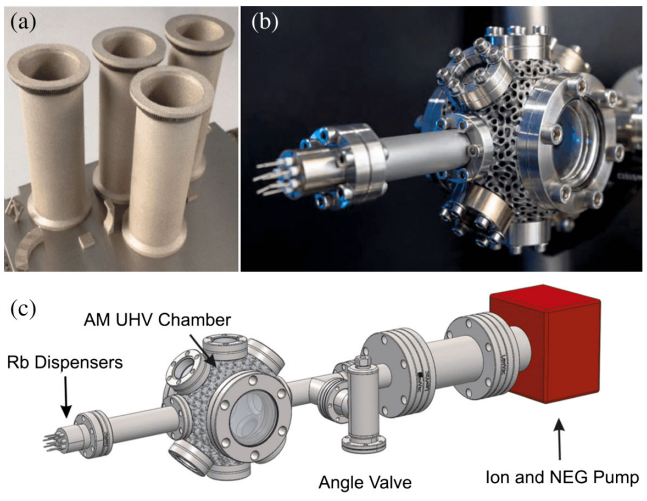

FIG. 32. (a) Additively manufactured DN40KF tubes [228], (b) vacuum chamber, and (c) UHV test setup [148].

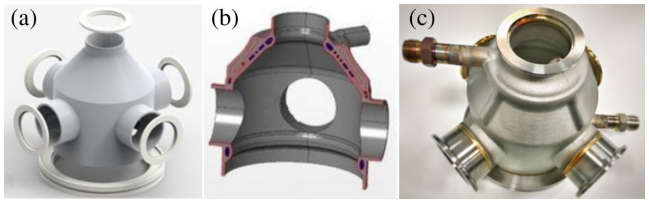

FIG. 33. (a) CAD model with (b) internal flow channels, and (c) photograph of the additively manufactured vacuum chamber after welding of standard vacuum components [229].

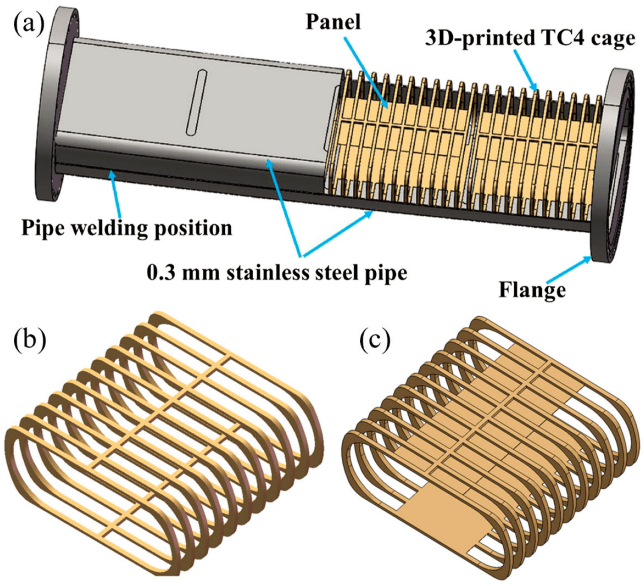

FIG. 34. CAD models of (a) thin-walled dipole-magnet vacuum chamber with internal stiffening cage, (b) initial cage design, and (c) cage design with additional cover panels for coupling impedance reduction [230].

flow channels into the cavity walls to facilitate heating during evacuation phase and cooling when needed during operation (Fig. 33). The design flexibility of AM was also leveraged by Du *et al.* [230] in developing a stiffening cage to be integrated into the thin-walled dipole-magnet vacuum chambers of the Booster Ring accelerator [Fig. 34(a)]. Two cover panels were added to the initial cage design [Figs. 34(b) and 34(c)] to mitigate beam coupling impedance, affecting beam quality and causing instabilities during high-intensity operation.

F. Heat exchangers and cooling systems

As demonstrated by the implementation of cooling systems into several accelerator components already discussed, typical applications that greatly leverage the opportunities offered by the design freedom of AM are represented by thermal management devices. Topological optimization can be harnessed to design components with improved heat transfer efficiency, for instance, by integrating intricate structures providing a large surface area for heat dissipation [38]. Of particular interest is the exploration of innovative heat exchanger designs incorporating triply periodic minimal surface (TPMS) structures, such as gyroids and lidinoids, which provide separated interpenetrating channels for efficient heat transfer between fluids at different temperatures [231].

In 2015, within the framework of the LIEBE project, Delonca [232] developed a novel design for Pb-Bi/water heat exchangers and employed PBF-LB/M to manufacture the first prototypes. In another investigation, Sciacca *et al.* [233] proposed three different heat sink configurations to be embedded in the backside of compact isotope-enriched targets used in the production of radionuclides for nuclear medicine. Two configurations consisted of lattice structures with different cell orientations relative to the inlet coolant flow, while the third configuration comprised individual helical twisted channels [Figs. 35(a) and 35(b)]. The prototypes were manufactured using PBF-LB/M with pure copper powder [Fig. 35(c)]. During experimental tests conducted in an in-house designed setup, all the samples exhibited good performance, with heat transfer coefficients exceeding 19 $\mathrm{kW\,m^{-2}\,K^{-1}}$. The higher dissipation capacity shown by the heat sink with the third configuration was attributed to the generation of vortices and secondary flows inside the twisted channels. Zhang *et al.* [234] also demonstrated the capability of topologically optimized cooling channels to reduce hot spot temperature (by ~24 °C) in 704.4 MHz CH copper cavities made by PBF-LB/M [Figs. 35(d)–35(f)], in comparison with the original design featuring nonconformal channels.

VI. SURFACE QUALITY IMPROVEMENT FOR ADDITIVELY MANUFACTURED ACCELERATOR COMPONENTS

The poor surface quality typically found in additively manufactured parts is a major concern for the application of AM in particle accelerators, as it is generally associated with limited UHV compatibility, sparse rf properties, and low breakdown strength. Moreover, because of their peculiar surface characteristics in both as-printed and postprocessed conditions, it remains uncertain whether established models and characterization techniques can reliably predict the performance of accelerator components produced by AM. For instance, Mayerhofer *et al.* [9] observed that the rf conductivity of additively manufactured linac cells surprisingly was not affected by the wavy pattern that appeared on their surface as a result of finishing operations, because its characteristic wavelength was much larger than the skin depth. Additionally, they noticed that the cell Q-factor could not be accurately predicted using classic gradient and Hammerstad models based on the measured root-mean-square roughness (Sq) values, suggesting the need to employ alternative measurement settings compared to those typically used for the assessment

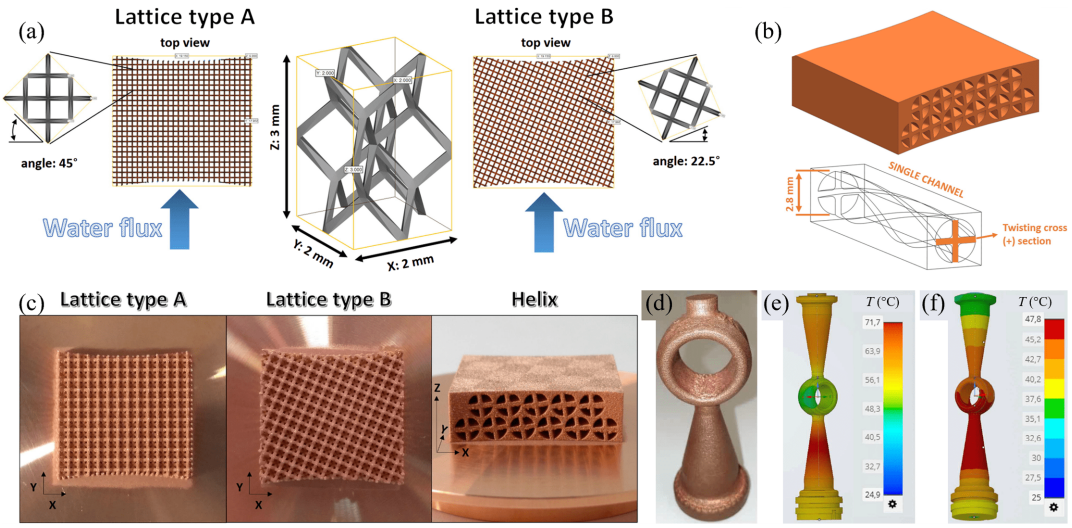

FIG. 35. Schematics of heat sinks with (a) lattice and (b) helical twisted channel configurations, (c) photograph of heat sink prototypes made by PBF-LB/M [233], and (d) photograph of additively manufactured 704.4 MHz CH cavity and results of thermal simulations with (e) conventional and (f) conformal cooling channels [234].

of conventionally manufactured rf structures. Khan *et al.* [235] also showed that the typical surface roughness of part made by PBF-LB/M exceeds the applicability range of the Groiss model, a modified version of the Hammerstad model for the prediction of the Q-factor of rf cavity resonators. On the other hand, the one-ball Hurey model, in which the surface is described as a nonuniform distribution of spheres of different sizes, provided more accurate predictions for both the Q-factor and the resonant frequency. In another study, Zhang *et al.* [234] highlighted the limitations of considering only macroscopic roughness when evaluating the performance of components subjected to intense electromagnetic fields, neglecting the major role played by nanoscale surface protrusions in promoting vacuum breakdown.

Regarding postprocessing methods, the applicability of conventional milling is restricted to relatively simple geometries accessible to the machining tools. More sophisticated postprocessing methods have been developed to enhance the surface quality of more complex parts [156–159], with some of them already applied to accelerator component prototypes produced by AM.

A. Mechanical treatments

Mechanical surface treatments rely on the use of abrasive media to remove or plastically deform the outer layer of material containing the peaks and valleys that contribute to surface roughness, leaving behind a smoother appearance [139]. These methods include, among others, various polishing and tumble finishing techniques [159].

Horn *et al.* [210] employed a magnetically driven polishing technique to reduce the roughness of the inner surface of a WR10 waveguide produced with PBF-EB. The waveguide was filled with a paste containing magnetic particles mixed with silicon carbide and alumina abrasive particles. An external magnet guided the magnetic particles along the workpiece, inducing the movement of the abrasive media. This process removed the asperities from the surface profile, reducing the average roughness from 36 to 5 μm after 10,000 polishing cycles, during which four types of abrasive media with progressively decreasing sizes were used.

Torims *et al.* [199] employed conventional and chemically assisted tumble finishing to enhance the surface quality of RFQ prototypes manufactured using PBF-LB/M. During the process, the workpieces were inserted into a barrel containing water and proprietary abrasive media and compounds provided by Rösler Italiana S.r.l. The finishing effect was achieved through the relative motion between the parts and the abrasive media inside the barrel [159]. A commercial MMP TECHNOLOGY® mechanical-physical-catalytic treatment was also tested. All procedures successfully met the requirement for average surface roughness ($R_a < 0.4$ μm). However, conventional finishing required a longer processing time and was less effective in removing deep valleys on the part surface, as mechanical abrasion mainly acted on protruding features. This challenge was not faced by the chemically assisted and MMP TECHNOLOGY® processes, which easily removed a relatively thick layer of material containing all surface defects.

In addition to conventional tumble finishing, Candela *et al.* [184] employed an internally developed vibro-tumbling process to smooth the inner surface of copper rf cavities made by PBF-LB/M. In the vibro-tumbling system [Fig. 36(a)], the cavity is gripped at the two ends and set into vibration by an eccentric vibrating motor [236]. The smoothing effect is achieved by the abrasive media and compounds introduced inside the cavity before assembly

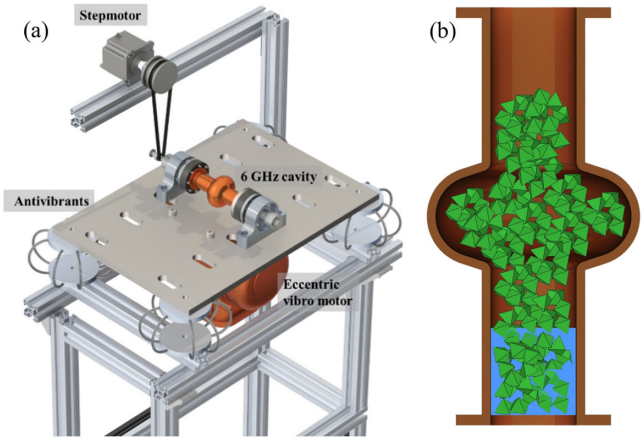

FIG. 36. (a) Schematic of vibro-tumbling system [236] and (b) rf cavity filled with abrasive media [237].

[Fig. 36(b)]. Following this process, the internal cavity surfaces presented a shiny appearance, and most of the macrodefects were successfully removed. A similar result was also achieved on additively manufactured SRF cavities made of pure niobium [14]. However, one of the copper parts broke at the iris during a second vibro-tumbling step, indicating the need to reinforce this region of the cavity structure, which demonstrated a concerning susceptibility to cracking during postprocessing operations [185].

B. Chemical and electrochemical polishing

Chemical polishing includes a variety of methods based on the use of chemical solutions that can globally treat the whole workpiece, with easy access to masked areas not reachable by solid media. Thus, they are particularly suited for the treatment of complex components with intricate geometries, such as lattice structures and internal cooling channels [159]. Electrochemical polishing additionally uses electrical current in combination with the etching action of chemical compounds. The workpiece is immersed in an electrolytic bath and is connected to the positive terminal of a dc power supply, serving as the anode of the electric circuit. When the current passes from the anode to the cathode, the peaks on the part surface are preferentially dissolved in the solution, as they feature a lower electrical resistance compared to the valleys, resulting in locally increased current intensity [139].

Candela *et al.* [139] employed both chemical and electrochemical methods to reduce the roughness of down-facing surfaces in copper samples produced by PBF-LB/M, following preliminary mechanical smoothening procedures. Chemical polishing was performed using SUBU5 etchant, part of the series of SUBU solutions developed at CERN for finishing copper rf cavities to be internally coated with thin superconducting niobium films [238]. These solutions contain sulfamic acid, n-butanol, hydrogen peroxide, and ammonium citrate in varying proportions. Both SUBU5 and electrochemical treatments produced mirrorlike surfaces, although the surface waviness resulting from the layer-wise fabrication was still clearly visible. A similar outcome, displaying reflective surfaces with macroroughness still evident, was observed in copper and niobium rf cavities electropolished in H_3PO_4/butanol and HF/H_2SO_4 bath, respectively [184,185].

In another study, Mayerhofer *et al.* [9] employed the Hirtisation® method, a combination of chemical and electrochemical treatments commercialized by RENA GmbH, to reduce the surface roughness of additively manufactured linac cells by an order of magnitude. Although a wavy pattern was still visible after the procedure, consisting of the iterative application of four Hirtisation® cycles, the process allowed setting the resonance frequency of the device with an accuracy of ~1 MHz. In addition, the unloaded Q-factor increased from 20%–25% to almost 75% of the simulated value.

C. Plasma electrolytic polishing

Plasma electrolytic polishing is a surface treatment based on material removal under the action of a plasma discharge [239]. The setup is similar to that used in electrochemical polishing processes, with the workpiece connected to a dc power supply as an anode and immersed in an electrolytic bath. However, the system operates at a much higher voltage regime [240]. An extremely intense current input is used to induce plasma physical reactions at the part surface, which include gas ionization, discharge bombardment, hydrothermal reactions, and metal dissolution. Electrochemical side processes also occur and contribute to the smoothening process [239].

In a series of publications, Chyhyrynets and colleagues [240–242] explored the opportunity to integrate plasma electrolytic polishing in the production routes of rf cavities and quadrupole resonators. Compared to more established chemical and electrochemical treatments, the plasma-based method allowed for achieving an optimal surface quality in about one-tenth the processing time. Additionally, a harmless electrolyte solution composed of dilute salts was used to process niobium prototypes, instead of the HF-containing solutions typically required in chemical and electrochemical processes for the reduction of stable niobium oxide surface layer [240]. Zhang *et al.* [234] first applied plasma electrolytic polishing to an additively manufactured accelerator component [the 704.4 MHz CH cavity shown in Fig. 35(d)], reducing the maximum peak-to-valley height R_z from ~80 to ~5 μm.

D. Laser smoothening

Various laser-based treatments have been developed to redefine the surface topography of metallic components produced by AM [159]. They involve the partial remelting of the outer layer of material under the action of a laser beam, aimed at removing surface defects and leaving

behind a homogeneous layer upon solidification. Zhao *et al.* [243,244] proposed laser polishing to achieve a bright finish on the inner surface of niobium SRF cavities, eliminating the need for aggressive chemical solutions typically employed in traditional chemical processes. Although their outcomes have not yet been extended to the postprocessing of additively manufactured accelerator components, research is currently underway to include this technology among possible alternatives to improve the surface quality of copper prototypes produced by PBF-LB/M [245,246].

E. Surface quality improvement through design optimization

Although additively manufactured parts typically require postprocessing operations to meet surface roughness standards, their surface quality can be improved to some extent by controlling the printing strategy and parameters. Adopting a contouring strategy, which uses different process parameters for the outer shell and the core region of the part [247], is often recommended.

Contouring takes into account the different solidification conditions experienced by the outer scanning tracks, which are surrounded by the loose powder bed, compared to the bulk tracks, which are adjacent to already consolidated material. Following the same principle, processing parameters can also be adjusted in PBF processes for the creation of downward-facing surfaces lying on the powder bed [139]. This also serves to obtain parts with a more homogeneous surface quality in the different regions, facilitating the following smoothing operations. Supports are usually needed to print features inclined at less than 45° relative to the build platform [139], to provide both mechanical stability and more efficient heat dissipation. However, removing these sacrificial structures can be challenging when fabricating small devices [141] and can leave macroscopic marks difficult to eliminate during surface finishing operations [142]. Part orientation during printing should be carefully selected to minimize the inclination of overhanging elements, reducing the need for support structures [140,142]. Also, when a self-support design is not feasible, support geometry should be topologically optimized to minimize the amount of sacrificial material and simplify removal procedures. Mayerhofer *et al.* [141] employed support structures composed of gradually tapering struts to fabricate 3 GHz rf cavities for medical linac devices (Fig. 37). This support geometry was designed to minimize the contact area with the cavity surface, thereby facilitating removal and finishing operations through a two-step Hirtisation® cycle. The combination of optimized support shape and surface treatment allowed for achieving the designed resonance frequency and Q-factor. A novel support design, involving contact-free conformal structures following the inner surface profile of the part, was also employed by Candela *et al.* [248] to manufacture niobium SRF cavities through PBF-LB/M. This internal structure allowed producing downfacing surfaces with an inclination angle of less than 30° and could be easily removed at the end of the process as it was separated from the cavity by a few layers of loose powder.

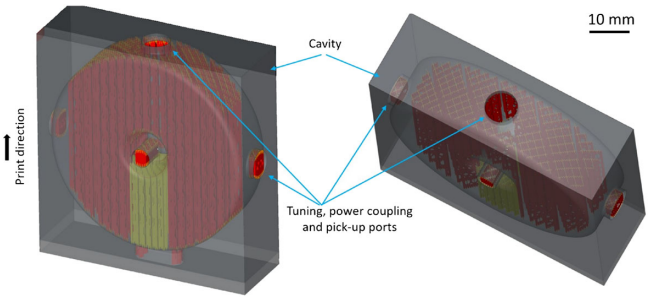

FIG. 37. CAD model of linac rf cavities (gray) with support structures (red and yellow) [141].

Khan [235] also investigated the influence of print design on the performance of additively manufactured rf cavities. He noted that to improve the Q-factor, the part should be oriented so as to minimize the roughness of the walls with higher surface current density, even though these represent a minor fraction of the total cavity surface. Therefore, aspects related to both the manufacturing process and the operating conditions should be synergistically considered for enhancing the surface quality of accelerator components made by AM through multiobjective design optimization.

VII. CONCLUSIONS AND OUTLOOK

The integration of additive manufacturing technologies into the fabrication routes of particle accelerator components represents a promising avenue to simplify the production processes, reduce costs and lead times, and enable novel designs inconceivable with conventional methods. This has the potential to foster the development of a new generation of more compact and accessible devices, with extended operational lifetimes and capable of pushing the current boundaries of high-energy physics research to new frontiers.

As outlined in this review, research on metal additive manufacturing has explored several applications within the field of particle accelerators. Prototypes of radio-frequency components, waveguides, beam intercepting devices, and vacuum systems have been successfully manufactured using metallic materials typically employed in accelerator applications, including pure copper, stainless steel, aluminum, and titanium alloys, as well as superconducting niobium and other refractory metals. Among the available metal additive manufacturing technologies, powder bed fusion methods have been predominantly employed owing to their ability to achieve high resolution and dimensional accuracy, even in geometrically complex parts, along with properties comparable with conventionally

processed materials. These processes use a powder feedstock material, which is deposited layer by layer and selectively melted according to the part geometry by means of a high-energy laser or electron beam. Direct energy deposition processes, in which the material is deposited only in the desired locations and simultaneously melted with a focused heat source (laser beam, electron beam, or electric arc), have seen a more limited use compared to powder bed fusion technologies due to their lower resolution and design flexibility. However, they offer advantages for creating additional features on existing parts, performing repairs, and fabricating multimaterial structures by varying the composition of the material delivered during the deposition process. Cold-spray additive manufacturing, which uses a compressed air gun to deposit metal or ceramic powders onto a substrate, has also shown promise for the production of multimaterial components for accelerator applications.

In numerous case studies, the monolithic fabrication enabled by additive manufacturing has yielded significant benefits in terms of costs and production time by avoiding the multiple machining and joining operations typical of conventional manufacturing methods. Additionally, the increased flexibility has facilitated the development of improved designs through topological optimization based on the functional requirements of the intended products. In particular, the integration of conformal cooling channels has enhanced heat dissipation in radio-frequency components operating at high frequencies, thereby preventing localized overheating and potentially enabling operation at higher powers and repetition rates. The implementation of lattice structure and varying wall thicknesses has been suggested as an effective means to reduce component weight while ensuring robust structural integrity.

Despite these encouraging outcomes, there are still open questions that need to be fully addressed to demonstrate additive manufacturing compliance with the stringent requirements typical of accelerator applications. These include the need for effective postprocessing to enhance the surface finish of printed parts and guarantee compatibility with ultrahigh vacuum, radio-frequency, and high-voltage environments, as well as established qualification protocols to ensure reliability under the extreme service conditions often encountered in accelerator applications. Furthermore, there is an emerging need for high-level design expertise to fully leverage the potential of additive manufacturing, overcoming the entrenched practices associated with conventional manufacturing processes.

These technical gaps are gradually being filled by continuous dedicated research and development efforts. Advanced postprocessing techniques are being developed to improve the surface quality of printed parts, even in areas with limited accessibility. Additionally, existing test setups and procedures are being adapted for the assessment of vacuum tightness, outgassing performance, and high-voltage holding of additively manufactured components.

Several research areas offer opportunities for further development in the near future. Advanced topological optimization based on thermomechanical, electromagnetic, and beam dynamics simulation tools may enable the development of more compact components capable of sustaining high accelerating gradient, to meet current demands for space-saving designs, increased energy efficiency, and reduced commissioning and maintenance costs. Promising prospects are also emerging for the seamless fabrication of multifunctional parts consisting of multiple materials, both metallic and ceramic. Investigation on AM methods for repairing damaged accelerator components also holds promise for reducing the operating costs and downtime of accelerator facilities.

ACKNOWLEDGMENTS

This work was conducted as part of the I.FAST project within the framework of the European Union's Horizon 2020 Research and Innovation programme under Grant Agreement No. 101004730 and is supported by the Latvian Council of Science under Grant Agreement No. VPP-IZM-CERN-2022/1-0001.

[1] H. Wiedemann, Introduction to accelerator physics, *Particle Accelerator Physics* (Springer, New York, 2015), 10.1007/978-3-319-18317-6_1.

[2] M. Durante, A. Golubev, W. Y. Park, and C. Trautmann, Applied nuclear physics at the new high-energy particle accelerator facilities, Phys. Rep. **800**, 1 (2019).

[3] C. Graeff, L. Volz, and M. Durante, Emerging technologies for cancer therapy using accelerated particles, Prog. Part. Nucl. Phys. **131**, 104046 (2023).

[4] P. A. Bystrov, A. V. Gordeev, A. Y. Kolokolova, M. A. Zavyalov, N. V. Ilyukhina, A. A. Molin, Y. S. Pavlov, S. P. Polyakova, A. V. Prokopenko, and V. P. Filippovich, Prospects of electron beam irradiation to ensure microbiological safety of food products, Phys. At. Nucl. **81**, 1526 (2018).

[5] M. I. Current, Ion implantation for fabrication of semiconductor devices and materials, in *Industrial Accelerators and Their Applications* (World Scientific, Singapore, 2012), p. 9, 10.1142/9789814307055_0002.

[6] More background on accelerators IAEA, https://www.iaea.org/topics/nuclear-science/nuclear-research/accelerators/background [accessed January 23, 2024].

[7] S. V. Kutsaev, Advanced Technologies for applied particle accelerators and examples of their use (review), Tech. Phys. **66**, 161 (2021).

[8] R. Aleksan, Future large scale accelerator projects for particle physics, Phys. Scr. **2013**, 014016 (2013).

[9] M. Mayerhofer, S. Brenner, R. Helm, S. Gruber, E. Lopez, L. Stepien, G. Gold, and G. Dollinger, Additive manufacturing of side-coupled cavity linac structures from pure copper: A first concept, Instruments **7**, 56 (2023).

[10] K. Scibor, S. Atieh, S. Mathot, P. Naisson, P. Richerot, and B. Bulat, PIXE-RFQ modulation and cavity machining, in *Proceedings of the Euspen's 20th International Conference Exhibition, Geneva* (2020), https://www.euspen.eu/knowledge-base/ICE20189.pdf.

[11] S. R. Ghodke, R. Barnwal, J. Mondal, A. S. Dhavle, S. Parashar, M. Kumar, S. Nayak, D. Jayaprakash, V. Sharma, S. Acharya, V. T. Nimje, K. C. Mittal, B. K. Dutta, and L. M. Gantayet, Machining and brazing of accelerating RF cavity, in *Proceedings of the 2014 International Symposium on Discharges and Electrical Insulation in Vacuum* (IEEE, New York, 2014), pp. 101–104, 10.1109/DEIV.2014.6961629.

[12] N. Delerue, A. Simar, R. L. Gerard, H. Carduner, S. Jenzer, P. Manil, and P. Repain, Prospects of additive manufacturing for accelerators, in *Proceedings of the 10th International Particle Accelerator Conference, Melbourne, Australia* (JACoW, Geneva, Switzerland, 2019), 10.18429/JACoW-IPAC2019-THPTS008.

[13] T. Torims, G. Pikurs, S. Gruber, M. Vretenar, A. Ratkus, M. Vedani, E. López, and F. Brückner, First proof-of-concept prototype of an additive manufactured radio frequency quadrupole, Instruments **5**, 35 (2021).

[14] S. Candela, M. Bonesso, V. Candela, R. Dima, G. Favero, A. Pepato, P. Rebesan, M. Romanato, E. Chyhyrynets, D. Ford, and C. Pira, Laser powder bed fusion of pure niobium for particle accelerator applications, in *Proceedings of the 14th International Particle Accelerator Confernce, IPAC-2023, Venice, Italy* (JACoW, Geneva, Switzerland, 2023).

[15] B. Blakey-Milner, P. Gradl, G. Snedden, M. Brooks, J. Pitot, E. Lopez, M. Leary, F. Berto, and A. du Plessis, Metal additive manufacturing in aerospace: A review, Mater. Des. **209**, 110008 (2021).

[16] R. Agustsson, P. Carriere, O. Chimalpopoca, V. A. Dolgashev, M. A. Gusarova, S. V. Kutsaev, and A. Y. Smirnov, Experimental studies of a high-gradient X-band welded hard-copper split accelerating structure, J. Phys. D. **55**, 145001 (2022).

[17] M. Leino, J. Pekkarinen, and R. Soukka, The role of laser additive manufacturing methods of metals in repair, refurbishment and remanufacturing—Enabling circular economy, Phys. Procedia **83**, 752 (2016).

[18] V. Shiltsev, A phenomenological cost model for high energy particle accelerators, J. Instrum. **9**, T07002 (2014).

[19] H. Bikas, P. Stavropoulos, and G. Chryssolouris, Additive manufacturing methods and modeling approaches: A critical review, Int. J. Adv. Manuf. Technol. **83**, 389 (2016).

[20] M. Laleh, E. Sadeghi, R. I. Revilla, Q. Chao, N. Haghdadi, A. E. Hughes, W. Xu, I. De Graeve, M. Qian, I. Gibson, and M. Y. Tan, Heat treatment for metal additive manufacturing, Prog. Mater. Sci. **133**, 101051 (2023).

[21] M. K. Thompson, G. Moroni, T. Vaneker, G. Fadel, R. I. Campbell, I. Gibson, A. Bernard, J. Schulz, P. Graf, B. Ahuja, and F. Martina, Design for additive manufacturing: Trends, opportunities, considerations, and constraints, CIRP Ann. **65**, 737 (2016).

[22] BS EN ISO/ASTM 52900:2021, Additive manufacturing—General principles—undamentals, and vocabulary (2021).

[23] T. DebRoy, H. L. Wei, J. S. Zuback, T. Mukherjee, J. W. Elmer, J. O. Milewski, A. M. Beese, A. Wilson-Heid, A. De, and W. Zhang, Additive manufacturing of metallic components—Process, structure and properties, Prog. Mater. Sci. **92**, 112 (2018).

[24] L. L. Myagkov, K. Mahkamov, N. D. Chainov, I. Makhkamova, I. V. Makarov, and S. V. Gasparyan, Conventional and advanced internal combustion engine materials, in *Alternative Fuels and Advanced Vehicle Technologies for Improved Environmental Performance* (Woodhead Publishing, Sawston, 2022), pp. 353–412, 10.1016/B978-0-323-90979-2.00008-1.

[25] V. Mishra, A. Babu, R. Schreurs, K. Wu, M. J. M. Hermans, and C. Ayas, Microstructure estimation and validation of ER110S-G steel structures produced by wire and arc additive manufacturing, J. Mater. Res. Technol. **23**, 3579 (2023).

[26] S. Yin, P. Cavaliere, B. Aldwell, R. Jenkins, H. Liao, W. Li, and R. Lupoi, Cold spray additive manufacturing and repair: Fundamentals and applications, Addit. Manuf. **21**, 628 (2018).

[27] BS EN ISO/ASTM 52911-1:2019 Additive manufacturing—Design, Part 1: Laser based powder bed fusion of metals (2019).

[28] W. Shi, Y. Liu, X. Shi, Y. Hou, P. Wang, and G. Song, Beam diameter dependence of performance in thick-layer and high-power selective laser melting of Ti-6Al-4V, Materials **11**, 1237 (2018).

[29] I. Yadroitsev, A. Du Plessis, and I. Yadroitsava, Basics of laser powder bed fusion, in *Fundamentals of Laser Powder Bed Fusion of Metals* (Elsevier, New York, 2021), pp. 15–38, 10.1016/B978-0-12-824090-8.00024-X.

[30] B. Brandau, A. Da Silva, C. Wilsnack, F. Brueckner, and A. F. H. Kaplan, Absorbance study of powder conditions for laser additive manufacturing, Mater. Des. **216**, 110591 (2022).

[31] C. Silbernagel, L. Gargalis, I. Ashcroft, R. Hague, M. Galea, and P. Dickens, Electrical resistivity of pure copper processed by medium-powered laser powder bed fusion additive manufacturing for use in electromagnetic applications, Addit. Manuf. **29**, 100831 (2019).

[32] M. Colopi, L. Caprio, A. G. Demir, and B. Previtali, Selective laser melting of pure Cu with a 1 kW single mode fiber laser, Procedia CIRP. **74**, 59 (2018).

[33] T. T. Ikeshoji, K. Nakamura, M. Yonehara, K. Imai, and H. Kyogoku, Selective laser melting of pure copper, JOM **70**, 396 (2018).

[34] S. D. Jadhav, L. R. Goossens, Y. Kinds, B. Van Hooreweder, and K. Vanmeensel, Laser-based powder bed fusion additive manufacturing of pure copper, Addit. Manuf. **42**, 101990 (2021).

[35] S. Gruber, L. Stepien, E. López, F. Brueckner, and C. Leyens, Physical and geometrical properties of additively manufactured pure copper samples using a green laser source, Materials **14**, 3642 (2021).

[36] K. Johnson, E. Burden, M. Shaffer, T. Noack, M. Mueller, J. Walker, E. MacDonald, P. Cortes, and J. Quintana, A copper pyramidal fractal antenna fabricated with green-laser powder bed fusion, Prog. Addit. Manuf. **7**, 931 (2022).

[37] I. Gibson, D. Rosen, B. Stucker, and M. Khorasani, Powder bed fusion, in *Additive Manufacturing Technologies* (Springer, Cham, 2021), pp. 125–170, 10.1007/978-3-030-56127-7_5.

[38] T. Romano and M. Vedani, Additive manufacturing of pure copper: Technologies and applications, in *Copper—From the Mineral to the Final Application* (IntechOpen, London, 2022), 10.5772/INTECHOPEN.107233.

[39] C. Cai and K. Zhou, Metal additive manufacturing, in *Digital Manufacturing – The Industrialization of Art to Part 3D Additive Printing* (2022), pp. 247–298, 10.1016/B978-0-323-95062-6.00005-X.

[40] A. Saboori, A. Aversa, G. Marchese, S. Biamino, M. Lombardi, and P. Fino, Application of directed energy deposition-based additive manufacturing in repair, Appl. Sci. **9**, 3316 (2019).

[41] A. Bandyopadhyay and B. Heer, Additive manufacturing of multi-material structures, Mater. Sci. Eng. **129**, 1 (2018).

[42] T. Romano, M. Abdelwahed, S. Bengtsson, F. Bruzzo, R. Casati, H. Gedda, E. López, P. Ulfberg, C. Wilsnack, and M. Vedani, Hybrid laser metal deposition of a Fe–Cr–Mo–V–Mn tool steel for hot stamping applications, Prog. Addit. Manuf. **8**, 1241 (2023).

[43] I. Gibson, D. Rosen, B. Stucker, and M. Khorasani, Material jetting, in *Additive Manufacturing Technologies* (Springer, Cham, 2021), pp. 203–235, 10.1007/978-3-030-56127-7_7.

[44] M. Winnicki, Advanced functional metal-ceramic and ceramic coatings, Coatings **11**, 1044 (2021).

[45] J. Upadhyay, J. Shoemaker, J. Bernardin, S. S. Kurennoy, J. Lyles, and K. Bishofberger, Additive manufacturing of copper RF structures for particle accelerator applications, in *Proceedings of the 14th International Particle Accelerator Conference, Venice, Italy* (JACoW, Geneva, Switzerland, 2023), 10.18429/JACoW-IPAC2023-MOOG3.

[46] J. Brandt, A review of ultrasonic additive manufacturing for particle accelerator applications, in *Proceedings of the 11th Mechanical Engineering Design of Synchrotron Radiation Equipment and Instrumentation, MEDSI2020, Chicago, IL* (JACoW, Geneva, Switzerland, 2021), pp. 185–188, 10.18429/JACoW-MEDSI2020-TUPC06.

[47] S. Roshchupkin, A. Kolesov, A. Tarakhovskiy, and I. Tishchenko, A brief review of main ideas of metal fused filament fabrication, Mater. Today Proc. **38**, 2063 (2021).

[48] R. J. Friel and R. A. Harris, Ultrasonic additive manufacturing—A hybrid production process for novel functional products, Procedia CIRP **6**, 35 (2013).

[49] B. Dutta, S. Babu, and B. Jared, *Additive manufacturing technology, Science, Technology and Applications of Metals in Additive Manufacturing* (Elsevier, New York, 2019), pp. 11–53.

[50] I. Gibson, D. Rosen, and B. Stucker, Sheet lamination processes, in *Additive Manufacturing Technologies* (Springer, New York, 2015), pp. 219–244.

[51] A. Mostafaei, A. M. Elliott, J. E. Barnes, F. Li, W. Tan, C. L. Cramer, P. Nandwana, and M. Chmielus, Binder jet 3D printing—Process parameters, materials, properties, modeling, and challenges, Prog. Mater. Sci. **119**, 100707 (2021).

[52] T. Romano, E. Migliori, M. Mariani, N. Lecis, and M. Vedani, Densification behaviour of pure copper processed through cold pressing and binder jetting under different atmospheres, Rapid Prototying J. **28**, 1023 (2022).

[53] M. Zago, N. Lecis, M. Mariani, O. U. Uçak, and I. Cristofolini, Influence of shape distortion on the precision of holes in parts fabricated by metal binder jetting, Int. J. Interact. Des. Manuf. (2023), 10.1007/s12008-023-01357-x.

[54] M. Kuchnir, Mechanical and thermal properties of structural materials, in *Handbook of Accelerator Physics and Engineering* (World Scientific, Singapore, 2013), pp. 399–403, 10.1142/9789814415859_0005.

[55] Q. Jiang, P. Zhang, Z. Yu, H. Shi, D. Wu, H. Yan, X. Ye, Q. Lu, and Y. Tian, A review on additive manufacturing of pure copper, Coatings **11**, 740 (2021).

[56] S. Sgobba, Vacuum for accelerators: Introduction to materials and properties, arXiv:2006.02212.

[57] S. Mathot *et al.*, The CERN PIXE-RFQ, a transportable proton accelerator for the machina project, Nucl. Instrum. Methods Phys. Res., Sect. B **459**, 153 (2019).

[58] T. Schietinger *et al.*, Commissioning experience and beam physics measurements at the SwissFEL Injector Test Facility, Phys. Rev. Accel. Beams **19**, 100702 (2016).

[59] G. Stancari, V. Previtali, A. Valishev, R. Bruce, S. Redaelli, A. Rossi, and B. S. Ferrando, Conceptual design of hollow electron lenses for beam halo control in the Large Hadron Collider (2014).

[60] P. L. E. M. Pasmans, D. C. Van Vugt, J. P. Van Lieshout, G. J. H. Brussaard, and O. J. Luiten, Extreme regimes of femtosecond photoemission from a copper cathode in a dc electron gun, Phys. Rev. Accel. Beams **19**, 103403 (2016).

[61] A. D. Cahill, J. B. Rosenzweig, V. A. Dolgashev, S. G. Tantawi, and S. Weathersby, High gradient experiments with X-band cryogenic copper accelerating cavities, Phys. Rev. Accel. Beams **21**, 102002 (2018).

[62] P. Frigola, R. Agustsson, S. Boucher, A. Murokh, J. Rosenzweig, G. Travish, L. Faillace, D. Cormier, and T. Mahale, A novel fabrication technique for the production of RF photoinjectors, in *Proceedings of the 11th European Particle Accelerator Conference, Genoa, Italy, 2008* (EPSAG, Geneva, 2008), pp. 751–753.

[63] G. E. Totten and D. S. Mackenzie, Annealing and recrystallization of coppers, Heat Treat. Nonferrous Alloy. **4**, 325 (2018).

[64] Y. Suetsugu, M. Shirai, M. Ohtsuka, T. Nishidono, K. Watanabe, Y. Suzuki, M. Tsuchiya, A. Yonemoto, K. Sennyu, and H. Hara, Development of copper-alloy Matsumoto–Ohtsuka-type vacuum flanges and its application to accelerator beam pipes, J. Vac. Sci. Technol. A **27**, 1303 (2009).

[65] L. Laurent, S. Tantawi, V. Dolgashev, C. Nantista, Y. Higashi, M. Aicheler, S. Heikkinen, and W. Wuensch, Experimental study of rf pulsed heating, Phys. Rev. ST Accel. Beams **14**, 041001 (2011).

[66] P. He, Accelerator vacuum technology challenges for next-generation synchrotron-light sources, in *Proceedings of the 8th International Particle Accelerator*

Conference, IPAC2017, Copenhagen, Denmark (JACoW, Geneva, Switzerland, 2017), pp. 4830–4835.

[67] M. Olsson, F. Lenrick, R. M'Saoubi, H. Larsson, A. Markström, I. Petrusha, J. E. Ståhl, and V. Bushlya, Study of wear mechanisms of cemented carbide tools during machining of single-phase niobium, Wear **450–451**, 203244 (2020).

[68] A. M. Valente-Feliciano, Superconducting RF materials other than bulk niobium: A review, Supercond. Sci. Technol. **29**, 113002 (2016).

[69] P. Maheshwari, F. A. Stevie, G. Myeneni, G. Ciovati, J. M. Rigsbee, and D. P. Griffis, Analysis of Interstitial elements in niobium with secondary ion mass spectrometry (SIMS), AIP Conf. Proc. **1352**, 151 (2011).

[70] H. Padamsee, Superconducting cavities from niobium-copper material, IEEE Trans. Nucl. Sci. **30**, 3354 (1983).

[71] A. Bianchi and W. V. Delsolaro, Temperature mapping on a niobium-coated copper superconducting radio-frequency cavity, Sci. Rep. **13**, 17075 (2023).

[72] S. Calatroni, 20 Years of experience with the Nb/Cu technology for superconducting cavities and perspectives for future developments, Physica (Amsterdam) **441C**, 95 (2006).

[73] D. Patel, S. H. Kim, W. Qiu, M. Maeda, A. Matsumoto, G. Nishijima, H. Kumakura, S. Choi, and J.vH. Kim, Niobium-titanium (Nb-Ti) superconducting joints for persistent-mode operation, Sci. Rep. **9**, 14287 (2019).

[74] P. Zhang, J. Li, Q. Guo, Y. Zhu, K. Yan, R. Wang, K. Zhang, X. Liu, and Y. Feng, NbTi superconducting wires and applications, in *Titanium for Consumer Applications: Real World Use of Titanium* (Elsevier, New York, 2019).

[75] E. Barzi and A. V. Zlobin, Nb_3Sn wires and cables for high-field accelerator magnets, in *Nb_3Sn Accelerator Magnets. Particle Acceleration and Detection*, edited by D. Schoerling and A. Zlobin (Springer, Cham, 2019).

[76] A. Ashraf, M. Mehmood, and S. A. Janjua, Study of ultra-high-vacuum properties of carbon-coated stainless steel beam pipes for high-energy particle accelerators, Arab. J. Sci. Eng. **44**, 6593 (2019).

[77] L. Sánchez, D. Carrillo, E. Rodríguez, F. Aragón, J. Sotelo, and F. Toral, Development of high precision joints in particle accelerator components performed by vacuum brazing, J. Mater. Process. Technol. **211**, 1379 (2011).

[78] J. Fang, Y. Hong, S. Wang, Y. Wang, B. Zhu, W. Zhang, B. Bian, and Y. Wang, Cryogenic secondary electron yield measurements on structural materials applied in particle accelerators, Nucl. Instrum. Methods Phys. Res., Sect. A **1027**, 166292 (2022).

[79] P. Fernández-Pisón, J. A. Rodríguez-Martínez, E. García-Tabarés, I. Avilés-Santillana, and S. Sgobba, Flow and fracture of austenitic stainless steels at cryogenic temperatures, Eng. Fract. Mech. **258**, 108042 (2021).

[80] T. Sakurai and O. Umezawa, Fracture toughness and martensitic transformation in type 316LN austenitic stainless steel extra-thick plates at 4.2 K, Mater. Sci. Eng. A **862**, 144122 (2023).

[81] M. K. Gupta, A. Priyadarshi, and Z. Khan, Hydrogen in stainless steel as killing agent for UHV: A review, Mater. Today Proc. **2**, 1074 (2015).

[82] V. Gómez, M. Wijnen, and J. Navarro-Cavallé, Direct thrust measurements of the HIPATIA system thruster unit, in *Proceedings of the 37th International Electric Propulsion Conference, IEPC-2022, Cambridge, MA, USA* (Electric Propulsion Society, USA, 2022).

[83] C. U. Lei, S. Ganjam, L. Krayzman, A. Banerjee, K. Kisslinger, S. Hwang, L. Frunzio, and R. J. Schoelkopf, Characterization of microwave loss using multimode superconducting resonators, Phys. Rev. Appl. **20**, 024045 (2023).

[84] Y. Reshitnyk, M. Jerger, and A. Fedorov, 3D microwave cavity with magnetic flux control and enhanced quality factor, Eur. Phys. J. Quantum Technol. **3**, 13 (2016).

[85] J. Jacob, P. Borowiec, A. D. Elia, G. Gautier, and V. Serrière, ESRF-EBS 352.37 MHz radio frequency system, in *Proceedings of the 12th International Particle Accelerator Conference, IPAC-2021, Campinas, SP, Brazil* (JACoW, Geneva, Switzerland, 2021), 10.18429/JACoW-IPAC2021-MOPAB108.

[86] M. Reagor, H. Paik, G. Catelani, L. Sun, C. Axline, E. Holland, I. M. Pop, N. A. Masluk, T. Brecht, L. Frunzio, M. H. Devoret, L. Glazman, and R. J. Schoelkopf, Reaching 10 ms single photon lifetimes for superconducting aluminum cavities, Appl. Phys. Lett. **102**, 192604 (2013).

[87] R. A. Michelotti, R. A. Tennant, N. K. Bultman, J. L. Uher, R. J. Brewton, and A. Mayer, Materials considerations for a high power-density accelerator, IEEE Trans. Nucl. Sci. **32**, 2849 (1985).

[88] S. Parashari, S. Mukherjee, B. K. Nayak, H. Naik, S. V. Suryanarayana, R. Makwana, and N. L. Singh, Excitation function of the ^{nat}Ti(p,x) ^{48}V, ^{47,46,44m}Sc reactions within the energy range of 10–22 MeV, Nucl. Phys. **A987**, 128 (2019).

[89] T. Ishida, E. Wakai, S. Makimura, P. G. Hurh, K. Ammigan, A. M. Casella, D. J. Edwards, D. J. Senor, C. J. Densham, M. Fitton, J. Bennett, D. Kim, N. Simos, M. Calviani, and C. Torregrosa Martin, Radiation damage studies on titanium alloys as high intensity proton accelerator beam window materials, J. Phys. Soc. Jpn. Conf. Proc. **28**, 041001 (2020).

[90] G. Bazzano, A. Ampollini, M. D. Astorino, F. Fortini, P. Nenzi, L. Picardi, C. Ronsivalle, E. Trinca, V. Surrenti, M. Vadrucci, E. C. R. Frascati, F. Borgognoni, E. C. R. Bologna, E. Nichelatti, E. C. R. Casaccia, and S. Maria, Electron beam qualification at ENEA Frascati particle accelerators laboratory, in *Proceedings of the 14th International Particle Accelerator Conference, IPAC-2023, Venice, Italy* (JACoW, Geneva, Switzerland, 2023), 10.18429/JACoW-IPAC2023-THPM127.

[91] J. C. Williams and R. R. Boyer, Opportunities and issues in the application of titanium alloys for aerospace components, Metals **10**, 705 (2020).

[92] R. Eichhorn, B. Bullock, B. Elmore, B. Clasby, F. Furuta, Y. He, G. Hoffstaetter, M. Liepe, T. O'Connell, J. Conway, P. Quigley, D. Sabol, J. Sears, E. Smith, and V. Veshcherevich, The Cornell main linac cryomodule: A full scale, high Q accelerator module for cw application, Phys. Procedia **67**, 785 (2015).

[93] N. Bazin and S. Chel, Cryomodule development for materials irradiation facilities: From IFMIF/EVEDA to IFMIF-DONES, in *Proceedings of the 20th International*

Conference on RF Superconductivity, SRF2021, East Lansing, MI (JACoW, Geneva, Switzerland, 2021), pp. 534–538, 10.18429/JACoW-SRF2021-WEPFAV001.

[94] T. L. Grimm, W. Hartung, M. Johnson, R. C. York, P. Kneisel, and L. Turlington, Cryomodule design for the rare isotope accelerator, in *Proceedings of the 20th Particle Accelerator Conference, PAC-2003, Portland, OR* (IEEE, New York, 2003), pp. 1350–1352, 10.1109/pac.2003.1289702.

[95] J. Guo, G. Lin, S. Cai, C. Xi, C. Zhang, W. Sun, Q. Wang, K. Yang, A. Li, Q. Wu, Y. Zhang, T. Xiang, R. J. Cava, and L. Sun, Record-high superconductivity in niobium–titanium alloy, Adv. Mater. **31**, 1 (2019).

[96] P. Kneisel, G. Ciovati, J. Sekutowicz, and L. Turlington, Progress on the development of a superconducting connection for niobium cavities, IEEE Trans. Appl. Supercond. **19**, 1416 (2009).

[97] C. F. Wu, Y. Tang, M. Tan, Q. Li, X. Chai, Y. Xu, K. Zhang, S. Zhang, L. Wang, W. Li, and G. Feng, Research of the 499.8 MHz superconducting cavity system for HALF, Nucl. Instrum. Methods Phys. Res., Sect. A **1050**, 168176 (2023).

[98] H. K. Zhang, Z. Yao, M. A. Kirk, and M. R. Daymond, Stability of Ni_3(Al, Ti) gamma prime precipitates in a nickel-based superalloy Inconel X-750 under heavy ion irradiation, Metall. Mater. Trans. A **45**, 3422 (2014).

[99] D. Raparia, Y. Y. Lee, J. Wei, and S. Henderson, Beam dump optics for the spallation neutron source, in *Proceedings of the 20th Particle Accelerator Conference, PAC-2003, Portland, OR* (IEEE, New York, 2003), pp. 3416–3418, 10.1109/pac.2003.1289933.

[100] G. Murdoch, A. Decarlo, S. Henderson, S. Kim, K. Potter, T. Roseberry, J. Rank, and D. Raparia, Beam dump window design for the spallation neutron source, in *Proceedings of the 20th Particle Accelerator Conference, PAC-2003, Portland, OR* (IEEE, New York, 2003), pp. 1467–1469.

[101] H. T. Bach, O. Anderoglu, T. A. Saleh, T. J. Romero, C. T. Kelsey, E. R. Olivas, B. H. Sencer, P. O. Dickerson, M. A. Connors, K. D. John, and S. A. Maloy, Proton irradiation damage of an annealed Alloy 718 beam window, J. Nucl. Mater. **459**, 103 (2015).

[102] D. A. McClintock, M. N. Gussev, C. Campbell, K. Mao, T. G. Lach, W. Lu, J. A. Hachtel, and K. A. Unocic, Observations of radiation-enhanced ductility in irradiated Inconel 718: Tensile properties, deformation behavior, and microstructure, Acta Mater. **231**, 117889 (2022).

[103] H. Wang, H. Jing, H. Qu, and J. Tang, Design of high-power graphene beam window, in *Proceedings of the 5th International Particle Accelerator Conference, IPAC2014, Dresden, Germany* (JACoW, Geneva, Switzerland, 2014), pp. 45–47, 10.18429/JACoW-IPAC2014-MOOCA03.

[104] P. McIntyre and A. Sattarov, On the feasibility of a tripler upgrade for LHC, in *Proceedings of the 21st Particle Accelerator Conference, Knoxville, TN, 2005* (IEEE, Piscataway, NJ, 2005), pp. 634–636, 10.1109/PAC.2005.1590511.

[105] P. Arpaia, M. Buzio, O. Capatina, K. Eiler, S. A. E. Langeslag, A. Parrella, and N. J. Templeton, Effects of temperature and mechanical strain on Ni-Fe alloy CRYOPHY for magnetic shields, J. Magn. Magn. Mater. **475**, 514 (2019).

[106] N. Templeton, T. Jones, S. Pattalwar, K. Marinov, A. May, E. Nolan, G. Burt, K. Artoos, R. Calaga, O. Capatina, T. Capelli, F. Carra, R. Leuxe, C. Zanoni, and A. Ratti, Design of the thermal and magnetic shielding for the LHC high luminosity crab-cavity upgrade, in *Proceedings of the 17th International Conference on RF Superconductivity, SRF2015, Whistler, BC, Canada* (JACoW, Geneva, Switzerland, 2015), pp. 1–5.

[107] S. Sah, G. Myneni, and J. Atulasimha, Experimental Characterization of Magnetic Materials for the Magnetic Shielding of Cryomodules in Particle Accelerators, IEEE Trans. Magn. **52**, 1 (2016).

[108] M. Scapin, C. Fichera, F. Carra, and L. Peroni, Experimental investigation of the behaviour of tungsten and molybdenum alloys at high strain-rate and temperature, EPJ Web Conf. **94**, 01021 (2015).

[109] M. V. Lungu, M. Lucaci, V. Tsakiris, A. Brătulescu, C. D. Cîrstea, M. Marin, D. Pătroi, S. Mitrea, V. Marinescu, F. Grigore, D. Tălpeanu, N. Stancu, P. Godeanu, and C. Melnic, Development and Investigation of tungsten copper sintered parts for using in medium and high voltage switching devices, IOP Conf. Ser. **209**, 012012 (2017).

[110] D. Obradors *et al.*, Characterization of the AMIT internal ion source with a devoted DC extraction test bench, in *Proceedings of the 8th International Particle Accelerator Conference, IPAC2017, Copenhagen, Denmark* (JACoW, Geneva, Switzerland, 2017), pp. 1740–1742.

[111] D. M. Goebel and A. C. Schneider, High-voltage breakdown and conditioning of carbon and molybdenum electrodes, IEEE Trans. Plasma Sci. **33**, 1136 (2005).

[112] R. Demellayer and J. Richard, High precision electro discharge machining of Molybdenum and Tungsten, Procedia CIRP. **6**, 89 (2013).

[113] S. Bini, B. Spataro, A. Marcelli, S. Sarti, V. A. Dolgashev, S. Tantawi, A. D. Yeremian, Y. Higashi, M. G. Grimaldi, L. Romano, F. Ruffino, R. Parodi, G. Cibin, C. Marrelli, M. Migliorati, and C. Caliendo, Molybdenum sputtering film characterization for high gradient accelerating structures, Chin. Phys. C **37**, 097005 (2013).

[114] T. Ramsvik, S. Calatroni, A. Reginelli, and M. Taborelli, Investigations of DC breakdown fields, in *Proceedings of the 10th European Particle Accelerator Conference, Edinburgh, Scotland, 2006* (EPS-AG, Edinburgh, Scotland, 2006), pp. 777–779.

[115] B. Wang, X. Hu, G. Zhou, J. Zhou, Y. Zhang, and Z. Zhang, Microstructures and properties of Tantalum/Molybdenum laser welding for electron guns, in *Proceedings of 19th International Conference on Vacuum Electronics (IVEC), Monterey, CA* (IEEE, New York, 2020), pp. 351–352, 10.1109/IVEC.2018.8391668.

[116] C. T. Martin, A. Perillo-Marcone, M. Calviani, L. Gentini, M. Butcher, and J. L. Muñoz-Cobo, Experiment exposing refractory metals to impacts of 440 GeV/c proton beams for the future design of the CERN antiproton production target: Experiment design and online results, Phys. Rev. Accel. Beams **22**, 013401 (2019).

[117] T. J. Horn and D. Gamzina, Additive manufacturing of copper and copper alloys, in *Additive Manufacturing Processes* (ASM International, OH, 2020), pp. 388–418 10.31399/ASM.HB.V24.A0006579.

[118] P. Kneisel, G. Ciovati, P. Dhakal, K. Saito, W. Singer, X. Singer, and G. R. Myneni, Review of ingot niobium as a material for superconducting radiofrequency accelerating cavities, Nucl. Instrum. Methods Phys. Res., Sect. A **774**, 133 (2015).

[119] A. Gurevich, Superconducting radio-frequency fundamentals for particle accelerators, Rev. Accel. Sci. Techol. **05**, 119 (2012).

[120] T. Junginger, S. Calatroni, A. Sublet, G. Terenziani, T. Prokscha, Z. Salman, A. Suter, T. Proslier, and J. Zasadzinski, A low energy muon spin rotation and point contact tunneling study of niobium films prepared for superconducting cavities, Supercond. Sci. Technol. **30**, 125013 (2017).

[121] Y. J. Jang, N. H. Kwon, S. H. Park, Y. Choi, H. Yu, K. B. Kim, D. W. Kim, and S. H. Choi, Activation evaluation of Siemens linear accelerator using Monte Carlo simulation, J. Korean Phys. Soc. **81**, 1107 (2022).

[122] Y. Ishikawa, T. Yoshimura, and M. Arai, Effect of surface oxide layers on deuterium permeation through stainless steels with reference to outgassing reduction in ultra-to extremely high vacuum, Vacuum **47**, 357 (1996).

[123] A. Korsbäck, F. Djurabekova, L. M. Morales, I. Profatilova, E. R. Castro, W. Wuensch, S. Calatroni, and T. Ahlgren, Vacuum electrical breakdown conditioning study in a parallel plate electrode pulsed dc system, Phys. Rev. Accel. Beams **23**, 033102 (2020).

[124] C. Ledford, C. Rock, P. Carriere, P. Frigola, D. Gamzina, and T. Horn, Characteristics and processing of hydrogen-treated copper powders for EB-PBF additive manufacturing, Appl. Sci. **9**, 3993 (2019).

[125] C. Pauzon, K. Dietrich, P. Forêt, S. Dubiez-Le Goff, E. Hryha, and G. Witt, Control of residual oxygen of the process atmosphere during laser-powder bed fusion processing of Ti-6Al-4V, Addit. Manuf. **38**, 101765 (2021).

[126] T. Romano, D. Krogere, A. Ratkus, H. Lauer, F. Marquardt, M. Vedani, D. Obradors, M. Weinmann, and T. Torims, Damage characterisation of tantalum ion source electrodes and reconditioning by wire- and powder-based laser metal deposition, Int. J. Refract. Met. Hard Mater. **116**, 106364 (2023).

[127] R. Douglas, R. Lancaster, T. Jones, N. Barnard, and J. Adams, The influence of powder reuse on the properties of laser powder bed-fused stainless steel 316L: A review, Adv. Eng. Mater. **24**, 2200596 (2022).

[128] F. Larini, R. Casati, S. Marola, and M. Vedani, Microstructural evolution of a high-strength Zr-Ti-modified 2139 aluminum alloy for laser powder bed fusion, Metals **13**, 924 (2023).

[129] K. T. Hartwig, J. Wang, D. C. Baars, T. R. Bieler, S. N. Mathaudhu, and R. E. Barber, Microstructural refinement of niobium for superconducting RF cavities, IEEE Trans. Appl. Supercond. **17**, 1305 (2007).

[130] N. Simos, H. G. Kirk, P. Thieberger, H. Ludewig, J. O. Conor, L. Mausner, P. T. Trung, K. T. McDonald, K. Yoshimura, and J. R. J. Bennett, Irradiation damage studies of high power accelerator materials, J. Nucl. Mater. **377**, 41 (2008).

[131] A. Zamiri, F. Pourboghrat, H. Jiang, T. R. Bieler, F. Barlat, J. Brem, C. Compton, and T. L. Grimm, On mechanical properties of the superconducting niobium, Mater. Sci. Eng. A. **435–436**, 658 (2006).

[132] B. Ding, Z. Yang, and X. Wang, Influence of microstructure on adielectric strength of CuCr contact materials in a vacuum, IEEE Trans. Components Packag. Manuf. Technol. Part A. **19**, 76 (1996).

[133] Y. Kok, X. P. Tan, P. Wang, M. L. S. Nai, N. H. Loh, E. Liu, and S. B. Tor, Anisotropy and heterogeneity of microstructure and mechanical properties in metal additive manufacturing: A critical review, Mater. Des. **139**, 565 (2018).

[134] A. Riihimäki, Outgassing studies of some accelerator materials, Ph.D. thesis, University of Helsinki, 2019.

[135] C. Zhao, N. D. Parab, X. Li, K. Fezzaa, W. Tan, A. D. Rollett, and T. Sun, Critical instability at moving keyhole tip generates porosity in laser melting, Science **370**, 1080 (2020).

[136] W. E. King, H. D. Barth, V. M. Castillo, G. F. Gallegos, J. W. Gibbs, D. E. Hahn, C. Kamath, and A. M. Rubenchik, Observation of keyhole mode laser melting in laser powder bed fusion additive manufacturing, J. Mater. Process. Technol. **214**, 2915 (2014).

[137] M. Leary, M. Khorasani, A. Sarker, J. Tran, K. Fox, D. Downing, and A. Du Plessis, Surface roughness, in *Fundamentals of Laser Powder Bed Fusion of Metals: A Volume in Additive Manufacturing Materials and Technologies* (2021), pp. 179–213.

[138] C. Emmelmann, D. Herzog, and J. Kranz, Design for laser additive manufacturing, in *Laser Additive Manufacturing: Materials, Design, Technologies, and Applications* (Woodhead Publishing, Sawston, 2017), pp. 259–279.

[139] V. Candela, M. Pozzi, E. Chyhyrynets, V. Garcia Diaz, S. Candela, R. Dima, G. Favero, C. Pira, A. Pepato, and P. Sonato, Smoothening of the down-skin regions of copper components produced via laser powder bed fusion technology, Int. J. Adv. Manuf. Technol. **123**, 3205 (2022).

[140] F. Calignano, Design optimization of supports for overhanging structures in aluminum and titanium alloys by selective laser melting, Mater. Des. **64**, 203 (2014).

[141] M. Mayerhofer, S. Brenner, M. Doppler, L. Catarino, S. Girst, V. Nedeljkovic-Groha, and G. Dollinger, Improving fabrication and performance of additively manufactured rf cavities by employing co-printed support structures and their subsequent removal, Instruments **8**, 18 (2024).

[142] Y. H. Kuo, C. C. Cheng, Y. S. Lin, and C. H. San, Support structure design in additive manufacturing based on topology optimization, Struct. Multidiscip. Optim. **57**, 183 (2018).

[143] W. Yuan, H. Chen, T. Cheng, and Q. Wei, Effects of laser scanning speeds on different states of the molten pool during selective laser melting: Simulation and experiment, Mater. Des. **189**, 108542 (2020).

[144] M. H. Nasab, A. Giussani, D. Gastaldi, V. Tirelli, and M. Vedani, Effect of surface and subsurface defects on fatigue behavior of AlSi10Mg alloy processed by laser powder bed fusion (L-PBF), Metals **9**, 1063 (2019).

[145] R. Gerard, Metal Additive Manufacturing—Overview of the process, mechanical processes and MME facility, PS Internal Dump review. PS_DUMPREVIEW_Metal_Additive_Manufacturing_RG. pptx (2016).

[146] F. Nuiry, G. Romagnoli, T. Polzin, E. Grenier Boley, and R. Gerard, 3D printing developments, PS Internal Dump core review (2016), https://indico.cern.ch/event/567462/contributions/2293345/attachments/1353055/2044370/3D_printing_developments.pdf.

[147] P. Romanescu, D. Omidvarkarjan, J. Ferchow, and M. Meboldt, Evaluation of the ultra-high vacuum suitability of laser powder bed fusion manufactured stainless steel 316L, in *Industrializing Additive Manufacturing. AMPA 2023, Springer Tracts in Additive Manufacturing* (2024), pp. 407–422.

[148] N. Cooper, L. A. Coles, S. Everton, I. Maskery, R. P. Campion, S. Madkhaly, C. Morley, J. O'Shea, W. Evans, R. Saint, P. Krüger, F. Oručević, C. Tuck, R. D. Wildman, T. M. Fromhold, and L. Hackermüller, Additively manufactured ultra-high vacuum chamber for portable quantum technologies, Addit. Manuf. **40**, 101898 (2021).

[149] J. Vovrosh, G. Voulazeris, P. Petrov, J. Zou, Y. Gaber, D. Woolger, M. M. Attallah, V. Boyer, and K. Bongs, Additive manufacturing of magnetic shielding and ultra-high vacuum flange for cold atom sensors, Sci. Rep. **8**, 1 (2018).

[150] G. Julien, Vacuum characterisation of 3D printed metals—Investigating the Additive Manufacturing process for a ultra high vacuum use, FCC Week **2017**, (2017), https://indico.cern.ch/event/556692/contributions/2487665/.

[151] A. Ratkus, T. Torims, G. Pikurs, V. Lacis, C. Garion, H. Kos, S. Rorison, S. Gruber, E. Lopez, L. Stepien, A. A. Patil, and M. Vedani, Evaluation of green laser source additive manufacturing technology for accelerator applications with ultra-high vacuum requirements, in *Proceedings of the 14th International Particle Accelerator Conference, IPAC-2023, Venice, Italy* (JACoW, Geneva, Switzerland, 2023) 4960–4963, 10.18429/JACoW-IPAC2023-THPM031.

[152] S. Haruyama, M. A. Choiron, and D. Nurhadiyanto, Optimum design of laminated corrugated metal gasket using computer simulation, Int. J. Integr. Eng. **11**, 29 (2019).

[153] R. Gumbleton, K. Nai, S. Hefford, and A. Porch, Effects of pt-processing treatmen ts on the microwave performance of additively manufactured samples, in *Proceedings of the 13th European Conference on Antennas and Propagation, EuCAP 2019, Krakow* (2019), pp. 1–4, https://ieeexplore.ieee.org/abstract/document/8740159.

[154] M. Mayerhofer, J. Mitteneder, and G. Dollinger, A 3D printed pure copper drift tube linac prototype, Rev. Sci. Instrum. **93**, 023304 (2022).

[155] M. Kellermeier, R. W. Assmann, K. Floettmann, F. Lemery, and W. Hillert, Dielectric loaded THz waveguide experimentally optimized by dispersion measurements, in *Proceedings of the 13th International Particle Accelerator Conference, IPAC2022, Bangkok, Thailand* (JACoW, Geneva, Switzerland, 2022), pp. 1526–1529, 10.18429/JACoW-IPAC2022-TUPOMS044.

[156] N. N. Kumbhar and A. V. Mulay, Post processing methods used to improve surface finish of products which are manufactured by additive manufacturing technologies: A review, J. Inst. Eng. Ser. C. **99**, 481 (2018).

[157] M. A. Mahmood, D. Chioibasu, A. U. Rehman, S. Mihai, and A. C. Popescu, Post-processing techniques to enhance the quality of metallic parts produced by additive manufacturing, Metals **12**, 77 (2022).

[158] X. Peng, L. Kong, J. Y. H. Fuh, and H. Wang, A review of post-processing technologies in additive manufacturing, J. Manuf. Mater. Process. **5**, 38 (2021).

[159] E. Maleki, S. Bagherifard, M. Bandini, and M. Guagliano, Surface post-treatments for metal additive manufacturing: Progress, challenges, and opportunities, Addit. Manuf. **37**, 101619 (2021).

[160] K. Kato, Y. Fukuoka, H. Saitoh, M. Sakaki, and H. Okubo, Effect of electrode surface roughness on breakdown conditioning under non-uniform electric field in vacuum, IEEE Trans. Dielectr. Electr. Insul. **14**, 538 (2007).

[161] Y. Inagawa, F. Miyazaki, K. Kato, M. Sakaki, H. Ichikawa, and H. Okubo, Effect of electrode surface roughness on breakdown conditioning process under non-uniform electric field in vacuum, in *Proceedings of the International Symposium on Discharges and Electrical Insulation in Vacuum, ISDEIV* (2004), Vol. 1, 72–75, 10.1109/DEIV.2004.1418604.

[162] A. Ratkus, T. Torims, G. Pikurs, V. Bjelland, S. Calatroni, R. Peacock, C. Serafim, M. Vretenar, W. Wuensch, M. Vedani, T. Romano, M. Pozzi, and M. F. Pedretti, Initial high electric field—Vacuum arc breakdown test results for additively manufactured pure copper electrodes, in *Proceedings of the 14th International Particle Accelerator Conference, IPAC-2023, Venice, Italy* (JACoW, Geneva, Switzerland, 2023), pp. 4957–4959, 10.18429/JACoW-IPAC2023-THPM030.

[163] I. Profatilova, X. Stragier, S. Calatroni, A. Kandratsyeu, E. Rodriguez Castro, and W. Wuensch, Breakdown localisation in a pulsed DC electrode system, Nucl. Instrum. Methods Phys. Res., Sect. A **953**, 163079 (2020).

[164] L. Waganer, Low cost fabrication approach for ARIES-CS coil structure, in *Proceedings of the ARIES Meeting* (2005), http://qedfusion.org/MEETINGS/0511/Waganer.pdf.

[165] L. M. Waganer, K. T. Slattery, and J. C. Waldrop, ARIES-CS coil structure advanced fabrication approach, Fusion Sci. Technol. **54**, 878 (2008).

[166] See Supplemental Material at http://link.aps.org/supplemental/10.1103/PhysRevAccelBeams.27.054801 for a list of publications on AM applied to particle accelerators.

[167] V. Dudnikov, Introduction, in *Development and Applications of Negative Ion Sources* (Springer, Cham, 2019), pp. 1–4, 10.1007/978-3-030-28437-4_1.

[168] M. Muramatsu and A. Kitagawa, A review of ion sources for medical accelerators (invited), Rev. Sci. Instrum. **83**, 02B909 (2012).

[169] P. Frigola, O. A. Harrysson, T. J. Horn, H. A. West, R. L. Aman, J. M. Rigsbee, D. A. Ramirez, L. E. Murr, F. Medina, R. B. Wicker, and E. Rodriguez, Fabricating copper components with electron beam melting, Adv. Mater. Process. **172**, 20 (2014).

[170] A. Girotto, M. Ballan, P. Rebesan, R. Dima, A. Monetti, I. Bodini, D. Paderno, V. Villa, A. Pepato, and

M. Manzolaro, Additively manufactured tantalum cathode for FEBIAD type ion sources: Production, geometric measurements, and high temperature test, J. Phys. Conf. Ser. **2687**, 082047 (2024).

[171] J. M. Davis, M. Saei, D. P. Mohanty, A. Udupa, T. Sugihara, and S. Chandrasekar, Cutting of tantalum: Why it is so difficult and what can be done about it, Int. J. Mach. Tools Manuf. **157**, 103607 (2020).

[172] T. Sahner, Metallic Additive Manufacturing @ CERN—Work done in the Mechanical & Materials Engineering (MME) group from 2013 to 2014, Chall. Addit. Manuf. High Energy Phys (2014), https://indico.cern.ch/event/333735/contributions/779099/attachments/651316/895585/WS_AM_05112014_V1.pdf.

[173] I. Novitski, J. Coghill, T. Beale, J. Bergeron, R. Davidoff, B. Oshinowo, S. Raje, D. Swanson, C. Wilson, and A. Zlobin, Using additive manufacturing technologies in high-field accelerator magnet coils, IOP Conf. Ser. Mater. Sci. Eng. **1241**, 012049 (2022).

[174] J. Ferchow, M. Biedermann, P. Müller, B. Auchmann, A. Brem, and M. Meboldt, Harnessing manufacturing elements to select local process parameters for metal additive manufacturing: A case study on a superconducting solenoid coil, Addit. Manuf. **46**, 102140 (2021).

[175] L. Faillace, L. Palumbo, B. Spataro, A. Fukasawa, B. D. O'Shea, J. B. Rosenzweig, and P. Frigola, An ultra-high repetition rate S-band RF gun, in *Proceedings of the 30th International Free Electron Laser Conference, FEL2008, Gyeongju, Korea* (JACoW, Geneva, Switzerland, 2008), pp. 282–284.

[176] L. Faillace, L. Palumbo, B. Spataro, A. Fukasawa, B. D. O'Shea, J. B. Rosenzweig, and P. Frigola, Experimental characterization of the RF gun prototype for the SPARX-FEL project, in *Proceedings of the International Particle Accelerator Conference, Kyoto, Japan, 2010* (ICR, Kyoto, 2010), pp. 3688–3690.

[177] R. B. Agustsson, S. M. Boucher, P. E. Frigola, A. Y. Murokh, J. B. Rosenzweig, and G. Travish, Method and apparatus for radio frequency cavity, U.S. Patent No. 7,411,361 (2008).

[178] L. Faillace, L. Palumbo, B. Spataro, A. Fukasawa, B. D. O'Shea, J. B. Rosenzweig, and P. Frigola, Development of an ultra-high repetition rate S-band RF gun for the SPARX project, in *Proceedings of the 23rd Particle Accelerator Conference, Vancouver, Canada, 2009* (IEEE, Piscataway, NJ, 2009), pp. 1815–1817.

[179] C. Nantista, D. Gamzina, C. Ledford, T. Horn, P. Carriere, and P. Frigola, Design and test of copper printed RF cavities, in *Proceedings of 21st International Conference on Vacuum Electronics (IVEC), Monterey, CA* (IEEE, New York, 2020), pp. 149–150.

[180] P. Frigola, R. Agustsson, L. Faillace, A. Murokh, G. Ciovati, W. Clemens, P. Dhakal, F. Marhauser, R. Rimmer, J. Spradlin, S. Williams, J. Mireles, P. A. Morton, and R. B. Wicker, Advance additive manufacturing method for SRF cavities of various geometries, in *Proceedings of the 17th International Conference on RF Superconductivity, SRF2015, Whistler, Canada* (JACoW, Geneva, Switzerland, 2015), pp. 1181–1184.

[181] C. A. Terrazas, S. M. Gaytan, J. Mireles, P. Frigola, D. Espalin, and R. B. Wicker, EBM fabrication and characterization of high purity niobium for superconductor application, in *2014 International Solid Freeform Fabrication Symposium* (University of Texas, Austin, 2014), pp. 605–616.

[182] C. A. Terrazas, J. Mireles, S. M. Gaytan, P. A. Morton, A. Hinojos, P. Frigola, and R. B. Wicker, Fabrication and characterization of high-purity niobium using electron beam melting additive manufacturing technology, Int. J. Adv. Manuf. Technol. **84**, 1115 (2016).

[183] R. Rimmer, P. E. Frigola, and A. Y. Murokh, Additive manufacturing method for SRF components of various geometries, U.S. Patent No. 9,023,765B1 (2015).

[184] V. Candela, S. Candela, M. Bonesso, P. Rebesan, R. Dima, G. Favero, A. Pepato, M. Pozzi, E. Chyhyrynets, D. Ford, and C. Pira, Additive manufacturing of 6 GHz seamless SRF copper cavities: Printing, surface treatments and performance investigations, in *Proceedings of the 14th International Particle Accelerator Conference, IPAC-2023, Venice, Italy* (JACoW, Geneva, Switzerland, 2023), pp. 4943–4946, 10.18429/JACoW-IPAC2023-THPM023.

[185] D. Ford, R. Caforio, E. Chyhyrynets, G. Keppel, C. Pira, S. Candela, M. Bonesso, V. Candela, R. Dima, G. Favero, A. Pepato, P. Rebesan, M. Romanato, and M. Pozzi, Additive manufacturing of pure niobium and copper using laser powder bed fusion for particle accelerator applications, in *Proceedings of the 21st International Conference on RF Superconductivity SRF2023* (JACoW, Geneva, Switzerland, 2023), pp. 872–875.

[186] A. Riensche, P. Carriere, Z. Smoqi, A. Menendez, P. Frigola, S. Kutsaev, A. Araujo, N. G. Matavalam, and P. Rao, Application of hybrid laser powder bed fusion additive manufacturing to microwave radio frequency quarter wave cavity resonators, Int. J. Adv. Manuf. Technol. **124**, 619 (2023).

[187] D. L. Creedon, M. Goryachev, N. Kostylev, T. B. Sercombe, and M. E. Tobar, A 3D printed superconducting aluminium microwave cavity, Appl. Phys. Lett. **109**, 032601 (2016).

[188] R. Casati, M. H. Nasab, V. Tirelli, and M. Vedani, Effect of different heat treatment routes on microstructure and mechanical properties of AlSi7Mg, AlSi10Mg and Al-Mg-Zr-Sc alloys produced by selective laser melting, in *Proceedings of the Euro PM 2018 Congress & Exhibition, Bilbao, Spain* (2020).

[189] G. Lupi, J. T. O. de Menezes, F. Belelli, F. Bruzzo, E. López, J. Volpp, E. M. Castrodeza, and R. Casati, Fracture toughness of AlSi10Mg alloy produced by direct energy deposition with different crack plane orientations, Mater. Today Commun. **37**, 107460 (2023).

[190] E. T. Holland, Y. J. Rosen, N. Materise, N. Woollett, T. Voisin, Y. Morris Wang, S. G. Torres, J. Mireles, G. Carosi, and J. L. Dubois, High-kinetic inductance additive manufactured superconducting microwave cavity, Appl. Phys. Lett. **111**, 202602 (2017).

[191] M. Mayerhofer, J. Mitteneder, C. Wittig, I. Prestes, E. Jägle, and G. Dollinger, First high quality drift tube Linac cavity additively manufactured from pure copper, in *Proceedings of the 14th International Particle*

Accelerator Conference, IPAC-2023, Venice, Italy (JACoW, Geneva, Switzerland, 2023), pp. 4968–4970, 10.18429/JACoW-IPAC2023-THPM035.

[192] C. Wehner, J. Merrick, B. Shirley, B. Weatherford, G. Mathesen, and E. Nanni, RF properties and their variations in a 3D printed klystron circuit and cavities (2022), http://arxiv.org/abs/2211.15500.

[193] C. Wehner, B. Shirley, G. Mathesen, J. Merrick, B. Weatherford, and E. A. Nanni, Radio Frequency properties of a 3D printed klystron circuit, Instruments **8**, 9 (2024).

[194] H. Hähnel, A. Ateş, B. Dedić, and U. Ratzinger, Additive manufacturing of an IH-Type Linac structure from stainless steel and pure copper, Instruments **7**, 22 (2023).

[195] H. Hähnel and U. Ratzinger, First 3D printed IH-type Linac structure—Proof-of-concept for additive manufacturing of Linac RF cavities, Instruments **6**, 9 (2022).

[196] H. Hähnel, A. Ateş, B. Dedić, and U. Ratzinger, Pure copper and stainless steel additive manufacturing of an IH-type Linac structure, in *Proceedings of the 14th International Particle Accelerator Conference, IPAC-2023, Venice, Italy* (JACoW, Geneva, Switzerland, 2023), pp. 4931–4934, 10.18429/JACoW-IPAC2023-THPM020.

[197] H. Hähnel and U. Ratzinger, First 3D printed IH-type Linac structure—Proof-of-concept for additive manufacturing of Linac RF cavities, in *Proceedings of the 12th International Particle Accelerator Conference, Campinas, SP, Brazil* (JACoW, Geneva, Switzerland, 2021), pp. 654–657, 10.18429/JACoW-IPAC2021-MOPAB194.

[198] H. Hähnel, A. Ateş, and U. Ratzinger, Update on the first 3D printed IH-type Linac structure—Proof-of-concept for additive manufacturing of Linac RF cavities, in *Proceedings of the 31st International Linear Accelerator Conference, LINAC2022, Liverpool, UK* (JACoW, Geneva, Switzerland, 2022), pp. 170–173, 10.18429/JACoW-LINAC2022-MOPOGE11.

[199] T. Torims, A. Ratkus, G. Pikurs, D. Krogere, M. Vretenar, A. Cherif, S. Gruber, E. Lopez, M. Pozzi, M. Foppa Pedretti, P. Wagenblast, M. Thielmann, M. Vedani, N. Delerue, and T. Otto, Evaluation of geometrical precision and surface roughness quality for the additively manufactured radio frequency quadrupole prototype, in *Proceedings of the 13th International Particle Accelerator Conference, IPAC2022, Bangkok, Thailand* (JACoW, Geneva, Switzerland, 2022), pp. 787–791 10.18429/JACoW-IPAC2022-TUOXSP3.

[200] TRUMPF, Radio frequency quadrupole made from pure copper. https://www.trumpf.com/en_INT/ [accessed February 9, 2024].

[201] D. Dollinger and M. Mayerhofer, Manufacturing method for radio-frequency cavity resonators and corresponding resonator, E.U. Patent No. EP 3 944 725 A1 (2020).

[202] A. Pepato, G. Favero, M. Bonesso, M. Romanato, P. Rebesan, R. Dima, V. Candela, S. Candela, F. Veronese, and P. Agostinetti, Implementation of the Additive Manufacturing for metals approach: The production of the acceleration grids for DTT NBI project, in *Proceedings of the 14th International Particle Accelerator Conference, IPAC-2023, Venice, Italy* (JACoW, Geneva, Switzerland, 2023), pp. 2230–2233, 10.18429/JACoW-IPAC2023-TUPM018.

[203] M. Bonesso, V. Candela, S. Candela, R. Dima, G. Favero, P. Rebesan, and A. Pepato, Laser powder bed fusion of CuCrZr for nuclear fusion acceleration components, in *Proceedings of the 14th International Particle Accelerator Conference, IPAC-2023, Venice, Italy* (2023), pp. 4896–4898, 10.18429/JACoW-IPAC2023-THPM024.

[204] G. L. D'Alessandro, Development of X-band High-Power RF load for CLIC applications using additive manufacturing techniques, Ph.D. thesis, European Organization for Nuclear Research (CERN), 2015.

[205] K. Lomakin, R. Guschlbauer, F. Osmanlic, Z. Fu, M. Sippel, K. Helmreich, C. Körner, M. Vossiek, and G. Gold, 3D Printed Copper Waveguides by Selective Electron Beam Melting Process for E-Band, in *Proceedings of the 49th European Microwave Conference (EuMC)* 774–777 (2019), 10.23919/EuMC.2019.8910893.

[206] G. Mathesen, C. Wehner, J. Merrick, B. Shirley, R. Agustsson, R. Berry, A. Diego, and E. Nanni, Utilization of additive manufacturing for the rapid prototyping of C-band radiofrequency loads, Instruments **7**, 23 (2023).

[207] A. Grudiev, Additive Manufacturing for X-band applications, CLIC14 Workshop (2014), https://indico.cern.ch/event/275412/contributions/1617680/.

[208] M. Colling, Developing an additively manufactured X-band RF load (2014), https://indico.cern.ch/event/320241/contributions/1698172/attachments/617452/849607/Developing_an_X-band_RF_load.pdf.

[209] N. Catalan-Lasheras, H. Damerau, R. Gerard, V. P. Romano, A. Grudiev, G. Mcmonagle, J. Paszkiewicz, S. Pitman, A. Solodko, I. Syratchev, B. Woolley, and W. Wuensch, High power conditioning of X-band RF components, in *Proceedings of the 9th International Particle Accelerator Conference, IPAC-2018, Vancouver, BC, Canada* (2018), pp. 2545–254810.18429/JACoW-IPAC2018-WEPMF074.

[210] T. Horn, I. Karakurt, C. Ledford, M. Gonzalez, D. Gamzina, N. C. Luhmann, L. Lin, U. C. Berkeley, and U. C. Davis, Additively manufactured WR-10 copper waveguide, in *2018 IEEE International Vacuum Electronics Conference (IVEC)* (2018), pp. 409–410, 10.1109/IVEC.2018.8391526.

[211] G. Lanza, C. Nantista, D. Gamzina, C. Ledford, T. Horn, P. Carriere, and P. Frigola, Outgassing of electron beam printed copper, in *Proceedings of the 2021 IEEE 22nd International Vacuum Electronics Conference, IVEC, Rotterdam, Netherlands* (IEEE, New York, 2021), 10.1109/IVEC51707.2021.9722518.

[212] A. Grudiev, Design of compact high power RF components at X-band, CLIC Note (2016), https://cds.cern.ch/record/2158484.

[213] H. Bursali, R. L. Gerard, A. Grudiev, O. Gumenyuk, P. M. Sanchez, and B. Riffaud, X-band RF spiral load optimization for additive manufacturing mass production, in *Proceedings of the 12th International Particle Accelerator Conference, IPAC-2021, Campinas, SP, Brazil* (JACoW, Geneva, Switzerland, 2021), pp. 1143–1146, 10.18429/JACoW-IPAC2021-MOPAB370.

[214] A. Grudiev, Development of X-band RF load using additive manufacturing, CLIC17 Workshop (2017), https://indico.cern.ch/event/577810/contributions/2485024/.

[215] A. Grudiev, Additive manufacturing for RF applications (2014), https://indico.cern.ch/event/333735/contributions/779090/attachments/651308/895576/Grudiev_-_Additive_Manufacturing_4RF_AG.pdf.

[216] R. Veness, N. Chritin, B. Dehning, J. Emery, J. H. Alvarez, M. Koujili, S. Samuelsson, and J. L. Sirvent, Design of a high-precision fast wire scanner for the SPS at CERN, in *Proceedings of IBIC2012, Tsukuba, Japan* (JACoW, Geneva, Switzerland, 2012).

[217] M. Koujili, B. Dehning, J. Koopman, D. Ramos, M. Sapinski, J. De Freitas, Y. Ait Amira, and A. Djerdir, Fast and high accuracy wire scanner, in *Proceedings of 9th European Workshop on Beam Diagnostics and Instrumentation for Particle Accelerators (DIPAC 2009), Basel, Switzerland* (CERN, Geneva, 2009), pp. 188–190.

[218] R. Veness, W. Andreazza, N. Chritin, B. Dehning, J. Emery, D. Gudkov, J. H. Alvarez, P. Magagnin, E. Piselli, and S. Samuelsson, Experience from the construction of a new fast wire scanner prototype for the CERN-SPS and its optimisation for installation in the CERN-PS booster, in *Proceedings of the 4th International Beam Instrumentation Conference, IBIC2015* (JACoW, Geneva, Switzerland, 2015), pp. 479–482.

[219] R. Veness, W. Andreazza, D. Gudkov, A. M. Marin, and S. Samuelsson, Metal 3D additive machining for in-vacuum beam instrumentation, in *Proceedings of the Mechanical Engineering Design of Synchrotron Radiation Equipment and Instrumentation, MEDSI2018, Paris, France* (JACoW, Geneva, Switzerland, 2018), pp. 121–124, 10.18429/JACoW-MEDSI2018-TUPH36.

[220] S. Jenzer, D. Auguste, J. Bonis, N. Delerue, F. Gauthier, A. Gonnin, O. Trofimiuk, and A. Vion, Study of the performances of a 3D printed BPM, J. Phys. Conf. Ser. **1067**, 082026 (2018).

[221] N. Delerue, D. Auguste, J. Bonis, F. Gauthier, S. Jenzer, and A. Moutardier, Tests of a 3D printed bpm with a stretched wire and with a particle beam, in *Proceedings of the 10th International Particle Accelerator Conference, Melbourne, Australia* (JACoW, Geneva, Switzerland, 2019), pp. 4368–4371, 10.18429/JACoW-IPAC2019-FRXXPLS1.

[222] F. Grazzi, C. Cialdai, M. Manetti, M. Massi, M. P. Morigi, M. Bettuzzi, R. Brancaccio, F. Albertin, T. Shinohara, T. Kai, A. Fedrigo, A. Di Giovanni, F. Arneodo, R. Torres, O. Al-Ketan, J. Elhashemi, F. Taccetti, and L. Giuntini, A multi-technique tomography-based approach for non-invasive characterization of additive manufacturing components in view of vacuum/UHV applications: Preliminary results, Rend. Lincei **32**, 463 (2021).

[223] K. Tavakoli, F. Alves, G. Baranton, Y. Benyakhlef, A. Berlioux, J. Dasilvacastro, M. E. Couprie, S. Ducourtieux, Z. Fan, C. Herbeaux, C. Kitegi, F. Lepage, A. Loulergue, V. Leroux, A. Mary, F. Marteau, A. Nadji, V. Pinty, M. Ribbens, A. Carcy, S. Pautatd, S. Thoraud, and A. Lejollec, Challenges and solutions for the mechanical design of SOLEIL-II, in *Proceedings of 11th Mechanical Engineering Design of Synchrotron Radiation Equipment and Instrumentation, Chicago, IL* (JACoW, Geneva, Switzerland, 2023).

[224] M. Sinico, G. Cogo, M. Benettoni, I. Calliari, and A. Pepato, Influence of powder particle size distribution on the printability of pure copper for selective laser melting, in *Proceedings of the 30th Annual International Solid Freeform Fabrication Symposium—An Additive Manufacturing Conference, Austin, TX* (University of Texas, Austin, 2019), pp. 657–667.

[225] R. Gerard, Fabrication Additive au CERN—Quelques exemples d'application (2018), https://indico.ijclab.in2p3.fr/event/4990/contributions/16695/attachments/13619/16418/I3DMetal_-_AMCERN.pdf

[226] C. Torregrosa, HRMT48-PROTAD Experiment and Relevance for BIDs, RaDIATE 2018 Collaboration Meeting (2018). https://indico.cern.ch/event/718767/contributions/3232507/.

[227] S. Chan, D. Cryer, and R. I. Price, Enhancement and validation of a 3d printed solid target holder at a cyclotron facility in Perth, Australia, Instruments **3**, 12 (2019).

[228] S. Jenzer, M. Alves, N. Delerue, A. Gonnin, D. Grasset, F. Letellier-Cohen, B. Mercier, E. Mistretta, C. Prevost, A. Vion, and J. P. Wilmes, Study of the suitability of 3D printing for ultra-high vacuum applications, in *Proceedings of the 8th International Particle Accelerator Conference, IPAC-2017, Copenhagen, Denmark* (JACoW, Geneva, Switzerland, 2017), pp. 3356–3358.

[229] C. R. Wolf, F. B. Beck, L. Franz, and V. M. Neumaier, 3D printing for high vacuum applications, in *Proceedings of the 22nd International Conference on Cyclotrons and their Applications, Cape Town, South Africa* (JACoW, Geneva, Switzerland, 2020), pp. 318–321, 10.18429/JACoW-Cyclotrons2019-THC04.

[230] S. Du, J. Liu, G. Zhu, J. Yang, J. Jiao, X. Zhang, G. Shen, J. Wu, C. Luo, and J. Meng, Measurement and optimization of the beam coupling impedance of a novel 3D-printed titanium alloy cage inside the thin-wall vacuum chamber, Rev. Sci. Instrum. **94**, 103308 (2023).

[231] H. Peng, F. Gao, and W. Hu, Design, modeling and characterization of triply periodic minimal surface heat exchangers with additive manufacturing, in *Proceedings of the 30th Annual International Solid Freeform Fabrication Symposium—An Additive Manufacturing Conference, Austin, TX* (2019), pp. 2325–2337.

[232] M. Delonca, LIEBE project: WP3-construction and tests, project coordination meeting (2015), https://indico.cern.ch/event/367917/contributions/1786366/attachments/731476/1003620/Melanie_LIEBE-WP3-coordinationmeeting-30012015.pdf.

[233] G. Sciacca, M. Sinico, G. Cogo, D. Bigolaro, A. Pepato, and J. Esposito, Experimental and numerical characterization of pure copper heat sinks produced by laser powder bed fusion, Mater. Des. **214**, 110415 (2022).

[234] C. Zhang, M. Heilmann, A. Japs, and C. Will, Development of a 704.4 MHz CH cavity using additive manufacturing, in *Proceedings of the 14th International Particle Accelerator Conference, Venice, Italy* (JACoW, Geneva, Switzerland, 2023), pp. 1744–1746, 10.18429/JACoW-IPAC2023-TUPA185.

[235] Q. M. Khan and D. Kuylenstierna, Analysis of Q-Factor for AM-SLM cavity based resonators using surface roughness models, IEEE J. Multiscale Multiphys. Comput. Tech. **9**, 75 (2024).

[236] E. Chyhyrynets, O. Azzolini, V. Garcia, G. Keppel, C. Pira, F. Stivanello, and L. Zanotto, Vibro-tumbling as an alternative to standard mechanical polishing techniques for SRF cavities, in *Proceedings of 19th International Conference on RF Superconductivity, SRF2019, Dresden, Germany* (JACoW, Geneva, Switzerland, 2019), pp. 464–466, 10.18429/JACoW-SRF2019-TUP026.

[237] INFN National Institute for Nuclear Physics, Tumbling and vibro-tumbling, https://surfacetreatments.infn.it/tumbling/ [accessed January 22, 2024].

[238] A. P. Rodríguez, L. M. A. Ferreira, and A. Sublet, Subu characterisation: Bath fluid dynamics vs etching rate, in *Proceedings of the 18th International Conference on RF Superconductivity, SRF-2017, Lanzhou, China* (JACoW, Geneva, Switzerland, 2017), pp. 575–579, 10.18429/JACoW-SRF2017-TUPB078.

[239] Y. Huang, C. Wang, F. Ding, Y. Yang, T. Zhang, X. He, L. Zheng, and N. Li, Principle, process, and application of metal plasma electrolytic polishing: A review, Int. J. Adv. Manuf. Technol. **114**, 1893 (2021).

[240] C. Pira, E. Chyhyrynets, R. Caforio, V. Garcia, O. Azzolini, G. Keppel, and F. Stivanello, Plasma electrolytic polishing as a promising treatment replacement of electropolishing in the copper and niobium substrate preparation for SRF, in *Proceedings of the 20th International Conference on RF Superconductivity, SRF2021, East Lansing, MI* (JACoW, Geneva, Switzerland, 2021), pp. 718–724, 10.18429/JACoW-SRF2021-THOTEV06.

[241] E. Chyhyrynets, O. Azzolini, R. Caforio, D. Fonnesu, D. Ford, G. Keppel, C. Pira, A. Salmaso, F. Stivanello, and G. Marconato, Plasma electrolytic polishing technology progress development for Nb and Cu substrate preparation, in *Proceedings of 21st Inernational. Conference on RF Superconductivity, SRF2023* (JACoW, Geneva, Switzerland, 2023), pp. 75–79, 10.18429/JACoW-SRF2023-MOPMB009.

[242] E. Chyhyrynets, O. Azzolini, R. Caforio, V. A. G. Diaz, G. Keppel, F. Stivanello, and C. Pira, Application of plasma electrolytic polishing onto SRF substrates, in *Proceedings of the 20th International Conference on RF Superconductivity SRF2021, East Lansing, MI* (JACoW, Geneva, Switzerland, 2021), pp. 116–120, 10.18429/JACoW-SRF2021-SUPTEV002.

[243] L. Zhao, J. M. Klopf, C. E. Reece, and M. J. Kelley, Laser polishing for topography management of accelerator cavity surfaces, Materwiss. Werksttech. **46**, 675 (2015).

[244] L. Zhao, J. M. Klopf, C. E. Reece, and M. J. Kelley, Laser polishing of niobium for superconducting radio-frequency accelerator applications, Phys. Rev. ST Accel. Beams **17**, 083502 (2014).

[245] V. Lacis, Laser polishing of additively manufactured RFQ prototype, in *Proceedings of the CERN Summer Student Programme* (2022), https://cds.cern.ch/record/2826408.

[246] V. Lacis, Research of surface post-treatment of additively manufactured pure copper parts using a laser beam, in *Proceedings of the 3rd CERN Baltic Conference CBC 2023* (2023), https://indico.cern.ch/event/1288731/contributions/5600882/.

[247] J. Gockel, L. Sheridan, B. Koerper, and B. Whip, The influence of additive manufacturing processing parameters on surface roughness and fatigue life, Int. J. Fatigue **124**, 380 (2019).

[248] S. Candela, P. Rebesan, D. De Bortoli, S. Carmignato, F. Zanini, V. Candela, R. Dima, A. Pepato, M. Weinmann, and P. Bettini, Pure niobium manufactured by laser-based powder bed fusion: Influence of process parameters and supports on as-built surface quality, Int. J. Adv. Manuf. Technol. **131**, 4469 (2024).